FEDERAL UNIVERSITY OF RIO GRANDE DO SUL
ENGINEERING SCHOOL
CONTROL AND AUTOMATION ENGINEERING

IGOR CAIKE GIRARDI DA VEIGA - 00218793

AERONAUTICAL DESIGN OF A CONVERTIBLE VTOL UNMANNED AERIAL VEHICLE

Porto Alegre
2021

IGOR CAIKE GIRARDI DA VEIGA - 00218793

AERONAUTICAL DESIGN OF A CONVERTIBLE VTOL UNMANNED AERIAL VEHICLE

Graduation Project presented to COMGRAD-CCA of Federal University of Rio Grande do Sul in partial fulfillment of the requirements for the degree of *Control and Automation Engineering*.

ADVISOR:
Prof. Dr. Mário Roland Sobczyk Sobrinho

Porto Alegre
2021

IGOR CAIKE GIRARDI DA VEIGA - 00218793

AERONAUTICAL DESIGN OF A CONVERTIBLE VTOL UNMANNED AERIAL VEHICLE

This Project was considered adequate for obtaining the credits of the course TCC (Diplom Project) of *Control and Automation Engineering* and approved in its final form by the Advisor and the Examination Committee.

Advisor: _____
Prof. Dr. Mário Roland Sobczyk Sobrinho, UFRGS
PhD. from UFRGS, 2009

Examination Committee:

Prof. Dr. Mário Roland Sobczyk Sobrinho, UFRGS
PhD. from UFRGS, 2009

Prof. Dr. Rogério José Marczak, UFRGS
PhD. from UFRGS, 2002

Prof. Dr. Renato Ventura Bayan Henriques, UFRGS
PhD. from UFMG, 2006

_____
Marcelo Götz
Course Coordinator
Control and Automation Engineering

Porto Alegre, May 2021.

ABSTRACT

Convertible unmanned aerial vehicles (CUAV) can fulfill complex missions automatically if a flight control system is available. The development of such systems requires a platform for tests and validation that presents the same dynamic behavior of an actual CUAV. The design of such aircraft includes challenges related to the combination of different flight dynamics as well as to unmanned flight. This work presents the complete aeronautical design of a CUAV aircraft which serves as a development platform for flight control systems. The proposed design is a vertical takeoff and landing (VTOL) aircraft with two flight modes: fixed-wing and rotary-wing. The aircraft development follows the classical aeronautical design path (conceptual design, preliminary design, and detailed design). Conceptual analysis is presented and the design trade-offs are discussed. A flying-wing tailsitter aircraft with a low aspect ratio, two motors, two ailerons, and a simple build is proposed. The performance is analyzed and the aircraft characteristics are defined following the typical aircraft design methodology. The aircraft components are designed, detailed, built, tested, and validated. The results include research and development related to CUAV-VTOL design, the proposed aircraft design itself, a prototype of the design, a mathematical model, and an open-loop maiden flight. In conclusion, credible CUAV-VTOL designs are possible, the obtained performance and flight characteristics of the proposed aircraft are acceptable, and the built prototype can be used as a development platform for flight control systems in future works.

Keywords: Aircraft design, UAV, VTOL, tailsitter.

RESUMO

Veículos aéreos não tripulados (VANT) conversíveis são capazes de atender missões complexas automaticamente se forem dotados de um sistema de controle de voo. O desenvolvimento de tais sistemas depende de uma plataforma de testes e validação que deve se comportar como um veículo aéreo não tripulado conversível. O projeto de tais aeronaves inclui questões únicas relativas à combinação de diferentes dinâmicas de voo, assim como questões específicas ao voo não tripulado. Este trabalho apresenta o projeto aeronáutico completo de uma aeronave não tripulada conversível que visa servir como uma plataforma de desenvolvimento de sistemas de controle de voo. A aeronave proposta é capaz de decolagem e pouso vertical e inclui dois modos de voo: asa-rotativa e asa-fixa. A aeronave é desenvolvida seguindo as três etapas clássicas de projeto aeronáutico (projeto conceitual, projeto preliminar e projeto detalhado). Uma análise conceitual é apresentada e os resultados das escolhas de projeto são analisados. Uma aeronave asa voadora *tailsitter* com baixa razão de aspecto, dois motores, dois ailerons e construção simplificada é proposta. A performance é analisada e características são definidas seguindo a metodologia típica de projeto aeronáutico. Os componentes da aeronave são projetados, detalhados, construídos, testados e validados. Os resultados incluem a pesquisa e desenvolvimento relativos a veículos aéreos não tripulados conversíveis, o projeto da aeronave proposta, um protótipo da aeronave, um modelo matemático e resultados de um voo inicial em malha aberta. Se concluiu que tal tipo de aeronave pode ser desenvolvida, que a performance obtida e as características de voo da aeronave proposta são aceitáveis e que o protótipo construído pode servir como plataforma de desenvolvimento de sistemas de controle de voo em trabalhos futuros.

Palavras-chave: projeto aeronáutico, VANT, VTOL, tailsitter.

CONTENTS

LIST OF FIGURES

LIST OF ABBREVIATIONS

AC	Aerodynamic center
AoA	Angle of attack
AR	Aspect ratio
CEIM	Commercial-off-the-shelf entertainment or industrial multicopter
CG	Center of gravity
CP	Center of pressure
CTOL	Conventional takeoff and landing
CUAV	Convertible unmanned aerial vehicle
DPA	Development platform aircraft
EPS	Expanded polystyrene
ESC	Electronic speed controller
EWF	Empty-weight fraction
L/D	Lift-to-drag (ratio)
LE	Leading edge
MTOW	Maximum take-off weight
PMMA	Polymethyl methacrylate
PVA	Polyvinyl acetate
RC/AHC	Radio-controlled aeromodelling hobbyist craft
Re	Reynolds number
RPM	Rotation per minute
STFP	Symmetric thin flat plate (airfoil)
t/c	Thickness-to-chord (ratio)
T/W	Thrust-to-weight (ratio)
TE	Trailing edge
UAV	Unmanned aerial vehicle
VTOL	Vertical takeoff and landing
VATOL	Vertical attitude takeoff and landing

LIST OF SYMBOLS

α	Angle of attack (AoA)
C_l	Airfoil lift coefficient
C_d	Airfoil drag coefficient
C_m	Airfoil pitching moment coefficient
$C_{x,\,max}$	Global maximum of given coefficient C_x
C_L	Wing lift coefficient
C_D	Wing drag coefficient
C_M	Wing pitching moment coefficient
θ	Pitch attitude angle
ϕ	Roll attitude angle (in rotary-wing mode)
ψ	Yaw attitude angle (in rotary-wing mode)
$\{X_C^P, Y_C^P, Z_C^P\}$	Pose frame coordinate axes system
W_0	Maximum take-off weight (MTOW)
W_{crew}	Crew weight
$W_{payload}$	Payload weight
W_{fuel}	Fuel weight
W_{empty}	Empty weight
$W_{battery}$	Battery weight
C_{x_y}	Derivative of given coefficient C_x with respect to variable y
C_{Di}	Wind induced drag coefficient
K	Induced-drag factor
e	Oswald efficiency factor
S_{ref}	Wing reference area
T_m	Total thrust
T_h	Horizontal component of thrust
$v_{max,\,D}$	Maximum horizontal speed regime considering drag force

$v_{max,\ L}$	Maximum horizontal speed regime considering operational lift force
ξ	Position vector composed of x, y, z.
$\{X_O^I, Y_O^I, Z_O^I\}$	Inertial frame coordinate axes system
$\{X_C^B, Y_C^B, Z_C^B\}$	Body frame coordinate axes system
η	Attitude vector composed of θ, ϕ, ψ.
L	Aerodynamic lift force
D	Aerodynamic drag force
M_w	Aerodynamic pitching moment
T_k	Thrust from motor $k = 1, 2$
δ_j	Deflection of aileron $j = 1, 2$ (in modeling)
$M^i_{\delta_j}$	Moment along i axis created by aileron j
ρ	Atmospheric density (ISA condition)
q	Dynamic pressure
V	Inertial speed
c	Wing chord
l_{AC}	Distance between CG and AC
l_m	Distance between a motor and CG
ω	Motor rotational speed
C_T	Propeller thrust coefficient
D_{prop}	Propeller diameter
Dev_{pw}	Flow development value
s	Distance between propeller and aileron
R	Propeller radius
V_{pw}	Propeller-induced speed
q_{pw}	Propeller-induced dynamic pressure
$S_{a,pw}$	Aileron surface inside propwash
S_a	Total aileron surface
l_a	Distance between the center of the aileron span and the CG
$l_{a,\ pw}$	Distance between the center of the span of $S_{a,pw}$ and the CG

1 INTRODUCTION

Any aircraft is designed to fulfill a specific mission. Such mission may be generic or include a set of requirements as range, speed, maneuvers, or flight conditions. Then, based on the defined mission the aircraft design is performed. Such a task is classically divided into three phases: conceptual design, preliminary design, and detailed design. The operation modes and layout characteristics selected in the aircraft design (or aeronautical design) are proposed as answers to each one of the requirements and their combined effect. Thus, each design is composed of a set of trade-offs (RAYMER, 1999).

Convertible aircraft are promising designs when generic missions are required due to the aircraft's capability to transition between different sets of characteristics. However, convertible aircraft are prone to more mechanical complexity, and in the case of a tailsitter, more difficult flight maneuvers. For example, to land the Convair XFY (the first tailsitter airplane) the pilot needed to look backwards to evaluate its own height and attitude while carefully working the throttle. This was exacerbated by the poor ergonomics the aircraft provided. The landing difficulty was the main cause of the contract cancellation and these concerns can be cited as examples of the difficulty for a human pilot to assess the attitude and position of the aircraft during the vertical flight as a tailsitter (CHANA; COLEMAN, 1996).

The utilization of unmanned aerial vehicles (or drones) spiked in all sectors of society in the last decades: in entertainment as a ludic tool due to its great mobility; in industry as a tool for inspection and transport; in defense as a craft enabling more advanced strategic warfare; and in the academy as platform for development of numerous subjects (mechanics, electronics, control, sensors, and state estimation). Nowadays, a handful of drone exists ranging in size and style: from the most notorious RC airplanes and quadcopters to unconventional layouts, experimental research projects, and military crafts.

Considering the difficulties of piloting a manned convertible aircraft and the expanded design space allowed by unmanned aircraft, a convertible unmanned aerial vehicle would be able to perform a variety of missions in peak performance while using closed-loop control. Aiming to analyze such kind of aircraft, this work presents the development of a convertible unmanned aerial vehicle focusing on the aeronautical design process. The expected result is a development platform aircraft (DPA) which answers to a generic mission and serves as a tool (or a development platform) for the study of the flight dynamics and the control systems of convertible unmanned aerial vehicles. Thus, the present work unfolds in the following specific objectives:

i Define a mission for the DPA;

ii Perform the aeronautical design based on the proposed mission;

iii Build a prototype of the DPA (the designed aircraft);

The remainder of this work is organized in the following manner: the chapter 2 provides a theory review on the main topics required to the aeronautical design of a convertible unmanned aerial vehicle; the aeronautical design is performed in chapter 3, chapter 4, and chapter 5; and the summary of the obtained results is presented in chapter 6. Furthermore, the reference frames are detailed in Appendix A, a mathematical model is proposed in Appendix B, and an open-loop maiden flight is reported in Appendix C.

For convenience, the phases of the aeronautical design are also introduced as a summary. In this work, the conceptual phase (chapter 3) presents the aircraft concept, discusses trade-offs, components, and defines the layout. In the preliminary phase (chapter 4), the initial sizing is performed, aerodynamic characteristics are defined, and the main parameters of the aircraft are estimated. In the detailed phase (chapter 5), all components (wing, powerplant, tail, and control surfaces) are defined, built, tested, and validated resulting in a prototype of the designed aircraft.

2 LITERATURE REVIEW

This chapter presents a literature review. First, concepts of aeronautics fundamental to aircraft design are revised. In the sequence, aircraft classification and operation are discussed. In the end, unconventional layouts are presented focusing on convertible unmanned aerial vehicles and their design and modeling.

2.1 Aerodynamics

Aerodynamics is the study of the dynamics of airflow, which includes the changing of velocity and pressure distributions when a body is placed within the airflow region. These changes generate forces and moments on the body, altering its motion state (ANDERSON, 2001).

Calculation of the aerodynamic forces on a body are performed in terms of two basic components: *lift*, which is perpendicular to the airflow direction, and *drag*, the parallel component. The magnitudes of these forces are affected by the angle between the body's reference line and the airflow direction, which is called the *angle of attack* (AoA) and commonly represented as α (ANDERSON, 2001). These definitions are shown schematically in Figure 1.

Figure 1: *Representation of lift, drag, and AoA.*

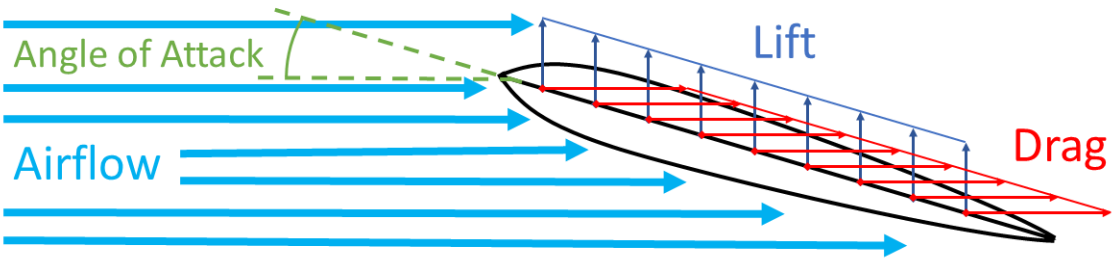

Source: Author.

The proportion between the lift force and the drag force is named *L/D ratio*. This ratio is an indicator of efficiency for a body aiming to produce lift. A higher L/D for the airfoil, the wing, or the whole airplane indicates a better flight performance in terms of range and endurance (ANDERSON, 2001).

2.1.1 Airfoil and Wing

The main geometric characteristics of a symmetric airfoil are the leading edge (LE) geometry (usually its radius), the trailing edge (TE) thickness, the thickness distribution,

the chord, and the ratio between maximum thickness and chord, known as *t/c ratio*. These characteristics are shown schematically on the left side of Figure 2 and they define the lift, drag, and pitching moment as a function of the AoA. These quantities can be defined in non-dimensional form through the use of aerodynamic coefficients: lift C_l, drag C_d, and pitching moment C_m (RAYMER, 1999).

Figure 2: *Geometric characteristics of an airfoil (left) and wing (right).*

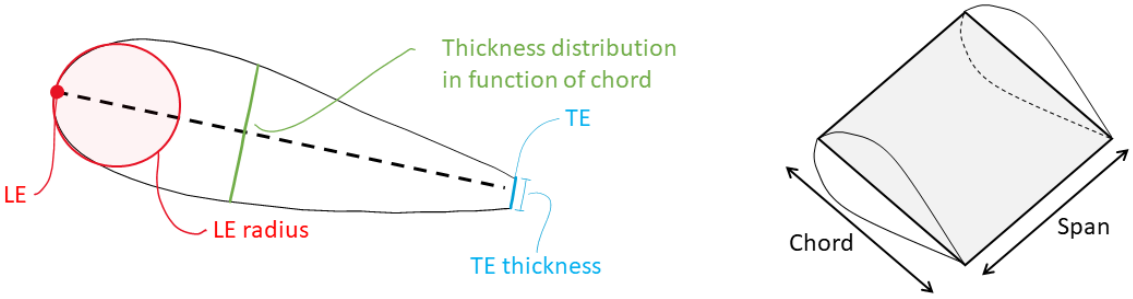

Source: Author.

Two points are relevant for airfoil stability: *center of pressure* (CP), which is defined as the equivalent action point of the distributed aerodynamic load (lift and drag); and *aerodynamic center* (AC) which is defined as the point about which the resultant moment is zero. Both CP and AC are characteristics of each airfoil. While CP may vary with AoA, AC remains static (ANDERSON, 2001).

Any symmetric airfoil produces lift when the AoA is different from zero. Experimental and theoretical data show that C_l varies linearly within small AoA. However, the linearity ends when flow separation starts at large AoA where $C_{l,\,max}$ is usually obtained. After such AoA, the flow separation on the upper surface of the airfoil causes a sudden decrease in the L/D ratio, a situation known as *stall* (ANDERSON, 2015).

The airfoil is a key characteristic of the wing (and the airplane) because its selection affects cruise speed, handling qualities, and the overall aerodynamic efficiency. The main geometric characteristics of a wing are the span (measured between wingtips) and the chord (measured between LE and TE). These characteristics are shown schematically in Figure 2. The relation between an airfoil (bidimensional, 2D) and its respective wing (tridimensional, 3D) is described mainly by one characteristic: the ratio between the span squared and the area of the wing which is known as *aspect ratio* (AR). Airplanes achieve the best aerodynamic efficiency with high AR wings because any 3D wing produces *induced drag* as a consequence of lift (RAYMER, 1999). Differently from the airfoil coefficients with lowercase, the wing aerodynamic coefficients are noted with uppercase subscripts: C_L, C_D, and C_M (ANDERSON, 2001).

2.2 Flying machines

A flying machine, or aircraft, can be classified as fixed-wing or rotary-wing. A fixed-wing aircraft (or airplane) produces aerodynamic lift through a wing placed inside an airflow. In contrast, a rotary-wing aircraft (or rotorcraft) lifts through the thrust created by power-driven rotors (ICAO, 1981).

The advantages of each class of aircraft derive from its lift source. A rotary-wing aircraft is capable of hover flight, point-to-point operation, and vertical takeoff and landing. However, as all its lift comes from motor thrust, the overall efficiency is smaller, limiting

speed, range, and endurance (RAYMER, 1999). On the other hand, a fixed-wing aircraft can perform missions with a larger maximum takeoff weight (MTOW) because a wing is the lift source. This implies bigger payload, endurance, range, and speed are available while needing a runway for takeoff and landing (WOODS, 1957).

In the context of the present work, two unconventional layouts for fixed-wing aircraft are relevant: *tailless airplane* and *flying-wing*. The first layout is an airplane designed without tail, empennage, and stabilizers (usually horizontal and vertical). The second layout is a tailless configuration which also omits a distinct fuselage. Such kind of design places the pilot, engines, and all compartments inside the wing. The flying-wing layout excels in L/D if compared to conventional layouts due to a smaller wetted area (RAYMER, 1999).

2.2.1 Takeoff and landing

For any fixed-wing aircraft, the takeoff and landing are the critical phases of flight when the mission does not include combat or weapons drop. The crucial importance of these phases is demonstrated statistically by the fact that they account for a high percentage of the accidents even though they represent only a small portion of the flight duration (BOEING, 2018). Moreover, the takeoff and landing phases represent a major security concern because of the interaction between the aircraft and the ground, the precise maneuvering required, the considerable accelerations present, and the low altitudes in which the maneuvers are executed (RAYMER, 1999).

An aircraft capable of vertical takeoff and landing (VTOL) is unaffected by most of the problems challenging the conventional takeoff and landing (CTOL) operation. Such aircraft admit various layouts: lighter-than-air airship, helicopter, and convertible plane. A *convertible plane* or *convertiplane* is any aircraft capable of changing its lift source during flight through diverse layouts: tiltrotor, vectored thrust with a jet engine, or tailsitter (RAYMER, 1999).

The *tailsitter* layout is relevant for the present work. Such configuration is also known as vertical attitude takeoff and landing (VATOL). In a tailsitter layout, the aircraft takes off and lands using its tail as support. While flying, a tailsitter aircraft transitions between rotary-wing mode and fixed-wing mode to perform different phases of its mission. The first tailsitter designs were two experimental prototypes commissioned by the US Navy in the 1950s: the Convair XFY "Pogo" and the Lockheed XFV "Salmon". Both aircraft required highly experienced pilots preventing its mainstream use (USN, 2009).

2.3 Unmanned aerial vehicle

An unmanned aerial vehicle (UAV) is an aircraft that flies without a pilot on board. Such aircraft is either remotely and fully controlled from another place (ground, another aircraft, space) or programmed and fully autonomous. Commercial-off-the-shelf entertainment or industrial multicopters (CEIM) and radio-controlled aeromodelling hobbyist crafts (RC/AHC) are also UAV (ICAO, 2011). A *drone* is a UAV that can perform at least some kind of automatic action on control and guidance. Those actions can be from low-level human pilot duties as attitude, speed, and flight path stabilization to high abstraction activities as waypoint following and target tracking (ESCARENO, 2008).

Usually, UAVs are employed in missions characterized as "dull, dirty, and dangerous" from a human pilot's perspective. Additionally, due to some attributes, UAVs can outperform a pilot's situational awareness and assessment (GUNDLACH, 2012):

- Orientation: in most manned designs pilots are upright, whereas in a UAV the sensors and avionics can be designed for a wide range of orientations;
- Visual sensors performance: human pilots can only see in the visual band with help of the neck to enlarge the forward hemisphere while in UAV this performance is a design criterion;
- Mathematical operations: while pilots have a limited ability to perform calculations in UAV designs this performance is also a design criterion.

As no crew weight is present in a UAV, the aircraft weight for the same payload can be reduced even if the aircraft layout is unaltered. This weight is larger than the crew weight itself as life support, safety, and comfort equipment are no longer needed. Moreover, in terms of design, UAVs offer an expanded design space because the unmanned flight allows for more efficient aircraft weight combined with unconventional layouts and relaxed (or even inexistent) physical constraints (ANDERSON, 2015).

The most common categorization for UAVs is based on size and weight. Micro aerial vehicles are limited to less than 1 m of wingspan and 0.45 kgf. The next tier is small UAVs between 0.45 kgf and 25 kgf which includes most CEIM and RC/AHC. Heavier UAVs compose a plethora of other tiers not listed here for brevity (GUNDLACH, 2012). Additionally, the manned aircraft categorization also applies: while most RC/AHC are fixed-wing aircraft, a CEIM is a rotary-wing aircraft.

An unmanned convertiplane is denominated a convertible unmanned aerial vehicle (CUAV). This type of aircraft combines the versatility of the convertiplanes (including the tailsitter) with the automatic actions on control and guidance of the UAVs (ESCARENO, 2008).

2.4 CUAV design, modeling and control

Many research efforts were made on the topic of CUAV. The work of (KNOEBEL et al., 2006) used a Pogo RC/AHC as a hardware platform to perform modeling, control architecture design, and trajectory study. Authors as (GREEN, 2005), (GREEN, 2006) and (FRANK et al., 2007) worked on enabling hover on a fixed-wing RC/AHC. Differently, authors as (STONE, 2002b) and (ESCARENO, 2008) present unique original designs of tailsitter UAV along with dynamics modeling, appropriate control schemes, and full VTOL flight results. Various works propose different control architectures for CUAV designs, notably (VERLING et al., 2016), (BARTH et al., 2020), and (SMEUR; BRONZ; CROON, 2020).

A UAV tailsitter design, or CUAV-VATOL, combines the best qualities of both flight modes without the complexity present in a manned VATOL as the Pogo, for example, in terms of pilot comfort and maneuvers (KNOEBEL et al., 2006). As a UAV, the comfort is taken aside from the analysis; and as the mathematical power and sensors arrangement are design criteria the complex maneuvers for takeoff and landing should be possible to be performed safely in an automated fashion (STONE, 2002b).

3 CONCEPTUAL DESIGN

This chapter presents the conceptual design of the DPA. First, a mission for the aircraft is defined. In the sequence, the conceptual trade-offs are discussed considering that the present work avoids innovation on structures or aerodynamics because the DPA is a development platform. The conceptual design considers three trade-off axes: fixed-wing performance, rotary-wing performance, and build-simplicity. The present work trades performance in both flight modes for build simplification. If required, rotary-wing performance is reduced in favor of the fixed-wing mode. In the end, the chosen conceptual design is presented.

3.1 Mission and concept

The concept of the DPA is based on the tailsitter VTOL (VATOL) designs from the 1950s, where the whole aircraft (including the control surfaces) is submerged in the propeller slipstream (propwash). In contrast to the classical tailsitters (the Pogo and the Salmon), the DPA uses electric motors instead of an internal combustion engine. In the same fashion as these classical designs, the DPA uses a tractor configuration with propellers. This setup causes the aircraft to fly in the turbulence from the propeller wake in fixed-wing mode, while the propwash enables the use of the control surfaces in low-speed rotary-wing flight.

The DPA is designed to answer to a simplified generic VATOL mission, without endurance requirements such as range or payload, and with flight times of just a few minutes. Likewise, no *high-performance maneuvers* are required, resulting in low-speed flights without dives, fast turns, or strong climbs. Therefore, the DPA mission is defined as a direct one-way flight in a windless environment without payload. The basic components of a flight plan configuring such a mission are:

a) Takeoff, hover and landing are performed in rotary-wing;

b) Displacements are possible in both rotary-wing and fixed-wing mode;

c) The first transition is always from rotary-wing to fixed-wing, being performed only after a successful takeoff;

d) The last transition is always from fixed-wing to rotary-wing, and it is a requirement for starting the landing procedure;

An example of a flight plan is shown in Figure 3 where takeoff, landing, and rotary-wing flight are depicted inside the green volumes, possible transitions within the red volumes, and fixed-wing cruise flight inside the blue volume.

Figure 3: *Example of flight plan compatible with the mission.*

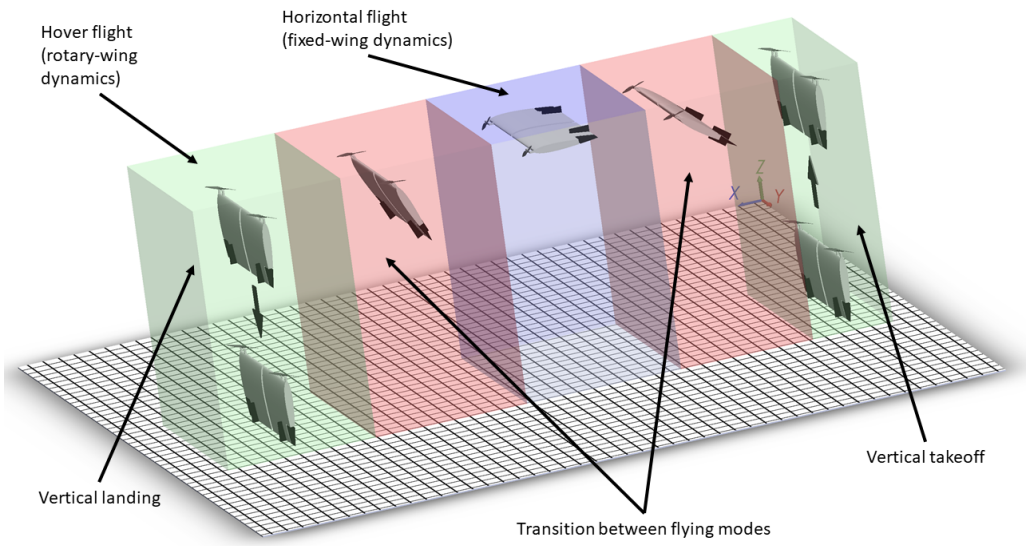

Source: Author.

The present work uses three reference frames to describe the aircraft's position and attitude: inertial, body and pose. The inertial frame is fixed to the ground, the body frame is fixed in the aircraft's center of gravity (CG), and the pose frame rotates with the aircraft around its CG. The three attitude angles are established considering the rotary-wing mode: pitch (θ), roll (ϕ), and yaw (ψ) are changed by moments around Y_C^P, X_C^P, and Z_C^P, respectively. This setup is presented in Figure 4 with the pose frame (in red) placed over a render of the DPA (considering the aircraft as per the end of the detailed design). These reference frames and the related measures are detailed in Appendix A.

Figure 4: *Reference frames and measures.*

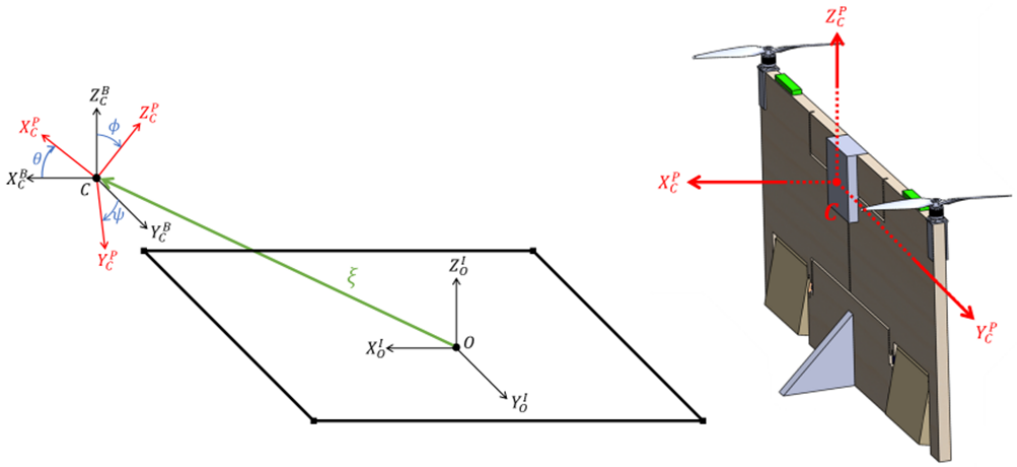

Source: Author.

In the present work, only the forward flight direction is considered due to the mission's characteristics. Thus, the pitch angle is always $\theta \in [0, -90°]$. This implies that in a forward flight in a windless environment (as required by the mission), the AoA and pitch are related as $\alpha = 90° + \theta$. The flight mode of the DPA is a continuous function of the lift source which is dependant on the current pitch angle. The vertical component of the thrust

is larger than the horizontal component if $\theta \in [0, -45°[$. Thus, for this pitch range, the motor thrust is the main source of lift and the DPA is in rotary-wing mode. Outside this range the aerodynamic wing lift becomes relevant and the DPA can be either in transition between flight modes or in fixed-wing mode.

3.2 Trade-offs and result

The aircraft components are analyzed to define the conceptual design: tail arrangement, body layout, motors, control surfaces, airfoil, and wing. Each component is briefly discussed, then *conceptual definitions* are presented to compose the chosen conceptual design which is shown in Figure 5 and Figure 6. Although the conceptual design is the *result* of the trade-off analysis, its early presentation is helpful in visualizing the interactions between the components. In the figures, the two dark gray regions are the control surfaces, the light gray body is the tail, and the blue region is the payload bay. In contrast to a typical airplane, CEIM, or RC/AHC, no evident top face or "up direction" is recognizable in the DPA. To avoid confusion, one face of the wing is selected arbitrarily as the top side during all phases of design, modeling, and maneuvers on the present work.

The DPA requires a stabilization structure to equilibrate the aircraft while on the ground. If the tail is such a structure, its geometry must be radially symmetric around the CG. However, the stabilization structure can also be distributed on the TE of the wing in a tailless layout. The first conceptual definition is the layout and tail: to achieve maximum L/D with a simple structure, the DPA uses a flying-wing layout without a central fuselage. Two bodies are installed in the TE at the top and bottom faces of the wing to act as the stabilization structure and vertical stabilizers without a rudder. Those bodies, called henceforth *tail* to avoid verbosity, are positioned in the center of the wingspan and create a left-right and top-bottom symmetry around the aircraft CG on top-view. As described by (RAYMER, 1999), the flying-wing layout requires a CG located close to the LE because no horizontal stabilizer is present.

Figure 5: *Top, frontal, and lateral views of the conceptual design.*

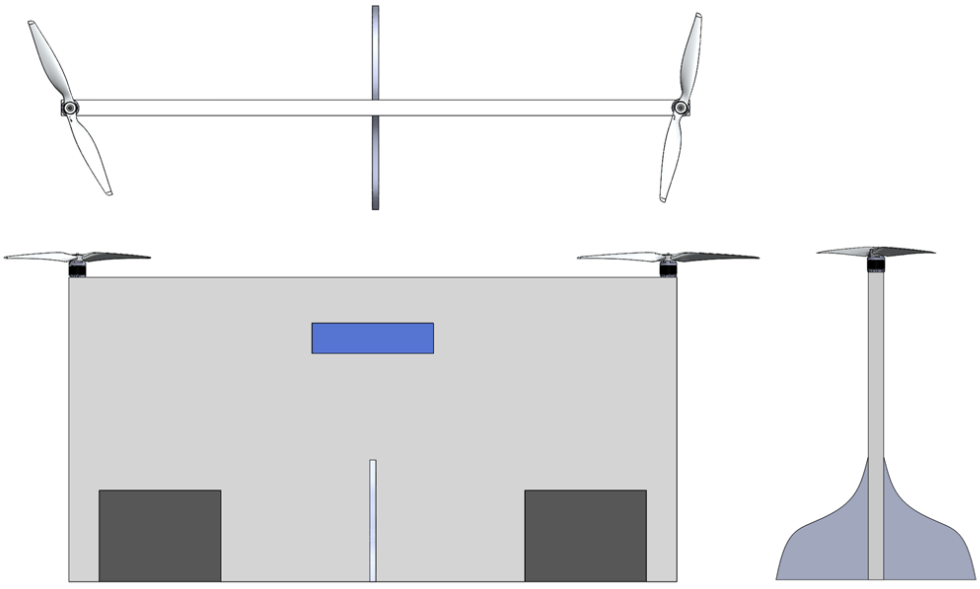

Source: Author.

As a CUAV, the definition of quantity and position of motors and control surfaces is analyzed considering the controllability and the effectiveness (named as *control authority*) of each attitude axes in both flight modes. As a flying-wing tailsitter, the thrust line is parallel to the wing chord. This setup implies that the motors are installed in the LE due to the limits on build-complexity. For this reason, the differential thrust from the motors actuates only along the X_C^P axis. In contrast, all the control surfaces of the DPA are located in the TE due to the flying-wing layout. This implies that the control surfaces actuate along the Y_C^P axis in common mode and along the Z_C^P axis in differential mode. Hence, to allow control over the three attitude axes at least two motors are required and at least one control surface in each half of the wingspan is required.

The control authority benefits from increases in lever arm around the CG for both the motors and the control surfaces. In contrast, the flow source is the main difference in control surfaces operation between the flight modes: in fixed-wing mode, the flight speed causes airflow over the control surfaces while in rotary-wing mode the propwash is the flow source. This causes less control authority to be available in rotary-wing mode. Such penalty can be reduced by placing the control surfaces along the propwash line. On the other hand, the placement of the control surfaces on the wingspan affects the L/D of the fixed-wing mode, because the disturbance they create on the airflow is amplified if the surface is placed on the wingtip. Additionally, the placement of the motors on the wingspan also affects the L/D of the fixed-wing mode, because in fixed-wing flight the motors act as a perturbation on the airflow due to the turbulent characteristics of the propwash. If the motors are installed close to the center of the wingspan, which is the section with more laminar airflow, the production of lift of the fixed-wing mode is drastically reduced. Thus, placing the motors close to the wingtip is favorable to the control of both flight modes and also for the aerodynamic performance of the fixed-wing mode. Therefore, the second conceptual definition is the attitude setup: the DPA uses two motors and two control surfaces. Identical motors are placed in the wingtip (left-right symmetric) and the control surfaces are placed close to the wingtips, but not exactly at them. Even thought, the control surfaces act as "elevons" in fixed-wing mode, they are called henceforth *ailerons* to avoid verbosity.

The airfoil represents a great deal on the build-complexity of a flying-wing prototype. The flat plate is the simplest airfoil to build. In comparison, conventional airfoils (either symmetric or asymmetric) highly increase the complexity. The third conceptual definition is the airfoil: the DPA uses a symmetric thin flat plate (STFP) airfoil because of the preference build-simplicity has over the performances.

Figure 6: *3D view of the conceptual design.*

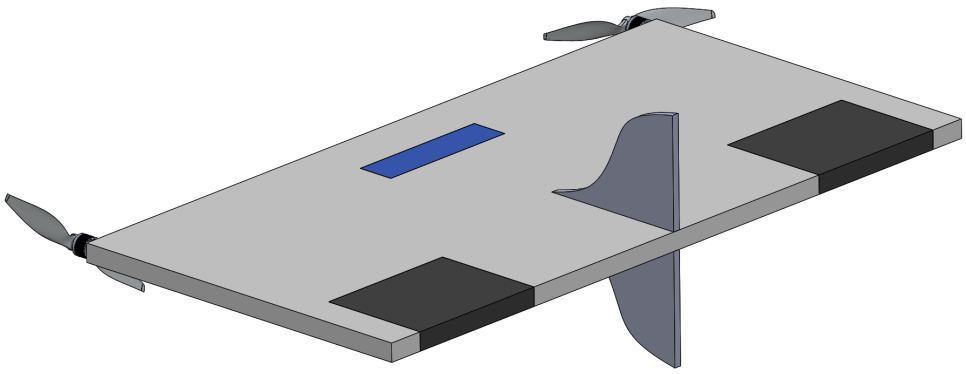

Source: Author.

The fixed-wing mode is the main affected by the wing geometry because it defines the maximum lift available. Twist, sweep, taper ratio, and wingtip devices (endplates or winglets) can improve the aerodynamic efficiency. However, only single-element airfoils and planar wings with cut-off tips are considered in the present work, allowing a streamlined build process. As a high AR is responsible for aerodynamic efficient wings, at least a ratio equal to the unit is recommended for fixed-wing aircrafts (RAYMER, 1999). In contrast, a low AR wing allows for a design with lighter requirements on structural strength over the wingspan whose reinforcements would contribute to a larger empty-weight. This compromise between AR and empty-weight is a common trade-off in conventional layout airplanes (ANDERSON, 2001). The fourth conceptual definition is the wing geometry: the DPA uses a low AR planar rectangular wing.

The fifth and last conceptual definition is the design-point, which defines the maximum battery weight as a requirement. The present work aims at a fixed-wing design-point in terms of wingspan, weight, and endurance of 1 m, 1 kgf, and 10 minutes. Various low-performance CEIM and small trainer fixed-wing RC/AHC are placed close to this design-point (FLOREANO; WOOD, 2015). The battery for the DPA is based on a typical cell pack for a fixed-wing RC/AHC close to the selected design-point. The maximum battery weight is 0.163 kgf which is the manufacturer-provided weight from a Zippy Compact 3S 25C 2200 mAh battery with a nominal voltage of 11.1 V.

4 PRELIMINARY DESIGN

This chapter presents the preliminary design of the DPA. First, a preliminary sizing is performed based on the design-point defined in the conceptual design. In the sequence, the performance metrics and the airfoil are analyzed. In the end, the AR is defined and the aerodynamic characteristics of the DPA's wing are estimated.

4.1 Preliminary sizing

The preliminary sizing establishes the DPA weight composition around the design-point defined in section 3.2 considering the selected battery. As the DPA has no payload, the total weight at takeoff is always equal to the MTOW. Due to the mission, the MTOW is estimated using a first-order method where it is divided in crew weight, payload weight, fuel weight, and empty weight (RAYMER, 1999). Each component is estimated through historical data trends allowing the MTOW (noted W_0) to be estimated as:

$$W_0 = \frac{W_{crew} + W_{payload}}{1 - (W_{fuel}/W_0) - (W_{empty}/W_0)} \tag{1}$$

In the DPA, the crew and the payload weights are zero and the fuel weight is the battery weight. Thus, the present work uses the battery as the payload establishing a reduced relation for the first-order method. Such relation, when inserted in Equation 1, defines the MTOW as a function of the battery weight and the empty-weight fraction (EWF):

$$W_0 = \frac{W_{battery}}{1 - (W_{empty}/W_0)} = \frac{0.163\ kgf}{1 - EWF} \tag{2}$$

As required, this setup allows for the MTOW to be estimated as a function of the battery weight which is defined based on the selected design-point. The EWF is dependant on the aircraft class and it is inversely proportional to the MTOW (RAYMER, 1999). In the present work, the EWF is estimated using historical data trends from design books. Then, openly available design data (of various UAV and VATOL) is used to validate the estimated EWF.

The works of (RAYMER, 1999) and (SADRAEY, 2012) present EWF of various fixed-wing aircraft classes. However, neither lightweight nor UAV design is available. To use the provided historical data trends some tailoring is required: the provided data trends are extrapolated to outside the typical MTOW range of each class, impractical values (EWF larger than 1.0) are dismissed, and the highest EWF is selected since the design is lightweight. Considering these conditions, an aircraft with an MTOW of 1 kgf (the design-point) has an EWF equal to 82%. In contrast, the work of (GUNDLACH, 2012)

presents data of lightweight UAV with the EWF ranging between 40% and 80% for fixed-wing designs and between 70% and 90% for rotary-wing designs. However, no CUAV design is available for direct comparison. Despite this fact and considering the presented ranges, the estimated EWF of 82% is acceptable for a CUAV because, since a rotary-wing dynamic is present, the EWF in a convertiplane should be higher than that of a fixed-wing aircraft for the same MTOW.

Using openly available data of various RC/AHC and CEIM, the EWF around the design-point is estimated as smaller than 80% for fixed-wing designs and larger than 60% for rotary-wing designs. Such ranges agree with the ones proposed by (GUNDLACH, 2012). Moreover, the EWF from the Pogo and the Salmon are estimated as close to 68% and 72%, respectively. As both the Pogo and the Salmon are heavier crafts, the EWF of the DPA should be at least higher than the two estimated values.

Considering all these values, the EWF of the DPA is selected as 82%. This implies that only 18% of the MTOW is battery weight. Using the relation defined in Equation 2, the preliminary MTOW of the DPA is calculated as 0.906 kgf with an empty-weight of 0.743 kgf considering a battery weight (as payload) of 0.163 kgf. The resultant preliminary MTOW matches the selected design-point.

4.2 Performance analysis

The preliminary performance of a fixed-wing aircraft is based on three main characteristics: the L/D ratio, the thrust-to-weight ratio (T/W), and the wing loading. In the present work, the T/W is defined as part of the preliminary design to allow vertical flight. However, the L/D and wing loading are outcomes of the design process as well as the various maximum and minimum speeds of the design.

Due to the mission, the DPA only operates inside a reduced flight envelope. This allows for the V-n diagram to be dropped, and for the selection of a constant load factor. The work of (RAYMER, 1999) indicates that the typical factor of safety for most aircraft is 1.5 with a load factor being included based on expected maneuvers and aircraft class. In the case of the DPA, an load factor equal to 1 is used with a reduced factor of safety equal to 1.25 (a 16% reduction) due to its mission and development platform characteristics.

The T/W of a rotary-wing aircraft must always exceed 1.0 to allow vertical flight. The DPA presents an excess thrust while in fixed-wing mode since the design is a CUAV-VATOL. This implies that any T/W estimated considering fixed-wing flight is superseded by the T/W required to enable VTOL. According to (GUNDLACH, 2012), the required T/W for a VTOL UAV is between three and five times the T/W of a CTOL design of the same MTOW. Moreover, the work of (RAYMER, 1999) sets VTOL T/W for manned aircraft as between 1.2 and 1.5 to achieve acceptable response in vertical acceleration, where 1.3 is a typical value and 1.5 defines an exceptional performance. The T/W of RC/AHC and CEIM varies widely: while a trainer fixed-wing RC/AHC has T/W as low as 0.25, acrobatic planes or racing drones have T/W larger than 2. Considering all these values, the preliminary T/W is selected as 1.3, yielding a required thrust of 1.1778 kgf (based on the preliminary MTOW).

4.3 Airfoil analysis

This section presents the aerodynamic characterization of the STFP airfoil selected for the DPA in section 3.2. As presented in (ANDERSON, 2001), the STFP airfoil has a

theoretical lift-curve slope equal to $\frac{dC_l}{d\alpha} = C_{l_\alpha} = 2\pi/\text{rad}$ and its CP and AC are located at the quarter-chord point. Additionally, the STFP airfoil (as any symmetric airfoil) produces no lift when AoA equals 0°. As discussed by (WINSLOW et al., 2017), the STFP airfoil has an aerodynamic performance invariant to the Reynolds number (Re) and it is more aerodynamic efficient than conventional airfoils in very-low-Re flow (below 10^5). Moreover, conventional airfoils present performance similar or better than the STFP airfoil in low-Re flow (between 10^5 and 10^6). The works of (WINSLOW et al., 2017) and (SELIG; GUGLIELMO, 1997) indicate the Re range from under 10^5 to 10^6 as pertinent to UAV applications. Thus, the present work defines such values as the DPA's Re range. This implies the selection of the STFP airfoil in the conceptual design trade-off instead of a conventional airfoil is not especially severe on fixed-wing performance.

The present work uses various sources for the aerodynamic coefficients of the STFP airfoil. The works of (WINSLOW et al., 2017), (SELIG; DONOVAN; FRASER, 1989), (PELLETIER; MUELLER, 2000), and (FAGE; JOHANSEN, 1927) provide data for small AoA and stall behavior. Such data defines the AoA range for fixed-wing flight as between 0 and 20°. Then, data from (SHELDAHL; KLIMAS, 1981) is used to extrapolate the behavior for AoA up to 90°, which comprises the remaining AoA range for forward flight direction. Such range serves for transition and for rotary-wing flight.

The reported performance of the STFP airfoil is quite diverse. All the data sources agree on values for C_d and also agree with the theoretical value in the linear region of the lift curve. However, the stall behavior and the plateau of C_l close to 20° AoA vary largely between the revised works. The present work aims at a conservative estimation of the aerodynamic performance. Hence, the established aerodynamic coefficients are based on all cited data sources considering the worst performance. The resulting coefficients for the fixed-wing AoA range of the STFP airfoil are presented on the left side of Figure 7 where no specific fixed-wing stall AoA is defined.

The extrapolated data for the upper AoA range is based on the NACA0009 airfoil reported by (SHELDAHL; KLIMAS, 1981). The NACA0009 airfoil presents better aerodynamic performance than the STFP airfoil in the fixed-wing AoA range. Thus, the present work defines the global maximum lift of the STFP airfoil as the plateau of the fixed-wing AoA range yielding $C_{l,\alpha=20°} \approx 0.71$. This implies that the lift performance only degrades for larger AoA. To obtain $C_{l,\alpha=90°} = 0$, two different lift-curve slopes are used changing at 45°. The C_d behavior of both airfoils is similar in the fixed-wing AoA range. In this range, the STFP airfoil has close to 10% higher drag than the NACA0009 airfoil. Considering this, the extrapolation for high AoA uses the same curve behavior as the NACA0009 airfoil, with an increase of 10% defining a $C_{d,\,max} = 2.0$ at 90° for the STFP airfoil. The aerodynamic coefficients of the STFP airfoil from 0 to 90° of AoA are shown on the right side of Figure 7.

Figure 7: *STFP airfoil aerodynamic coefficients.*

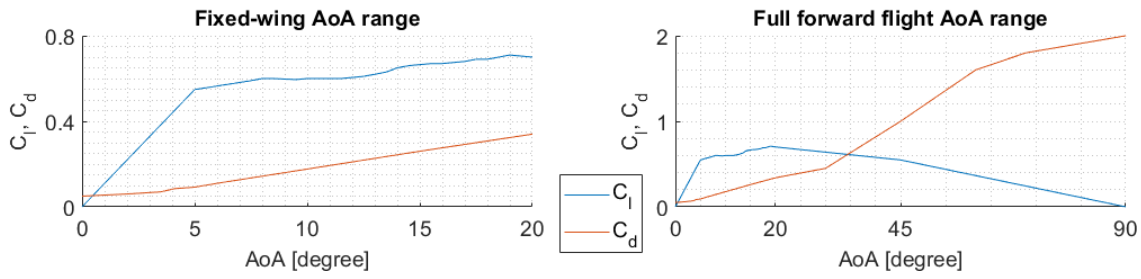

Source: Author.

4.4 Wing planform analysis

Various methods are available to estimate the performance of a wing. The present work uses a first-order method derived from (RAYMER, 1999) and (ANDERSON, 2001). In such method, a *lift-efficiency factor* defined as C_L/C_l is estimated through aerodynamic data trends. Then, the lift-efficiency factor scales the C_l of each AoA to define the wing C_L. This causes the C_L curve to be a small-scale version of the C_l curve which maintains the stall characteristics of the wing identical to the airfoil. Besides, the method defines the wing drag (C_D) as the sum of airfoil drag and induced drag (noted C_{Di}):

$$C_D = C_d + C_{Di} = C_d + K \cdot C_L^2 \tag{3}$$

where

$$K = \frac{1}{\pi \, e \, AR} \tag{4}$$

is known as *induced-drag factor* in where the *Oswald efficiency factor* (noted e) ranges from 0.7 and 0.85 for subsonic crafts (RAYMER, 1999).

The trade-off performed in this section analyses low AR wings to define the AR for the DPA's wing. The low AR range is between 1 and 3 if the wing is planar rectangular without tapper ratio nor sweep (RAYMER, 1999). The lift performance is defined by the lift-efficiency factor which is calculated for the AR range using data from (RAYMER, 1999). The drag performance is defined by the induced drag factor which is a function of the Oswald efficiency factor. The present work applies a 15% penalty over the worst e recommended by (RAYMER, 1999), resulting in a $e = (1-0.15) \cdot 0.7 \approx 0.6$. The resulting factors as a function of AR are shown on the left side of Figure 8.

In addition to the two typically used factors, the present work proposes other metrics to directly compare the performance of different AR. The *average drag from lift ratio* is calculated through the average of the percentages of the C_l created as C_{Di} at each AoA in the fixed-wing AoA range. In contrast, the *factor L/D ratio* is obtained by dividing the square of the lift-efficiency factor by the induced-drag factor providing a sort of equivalent-L/D ratio. The results are shown on the right side of Figure 8.

Figure 8: *Lift and drag performance as a function of AR.*

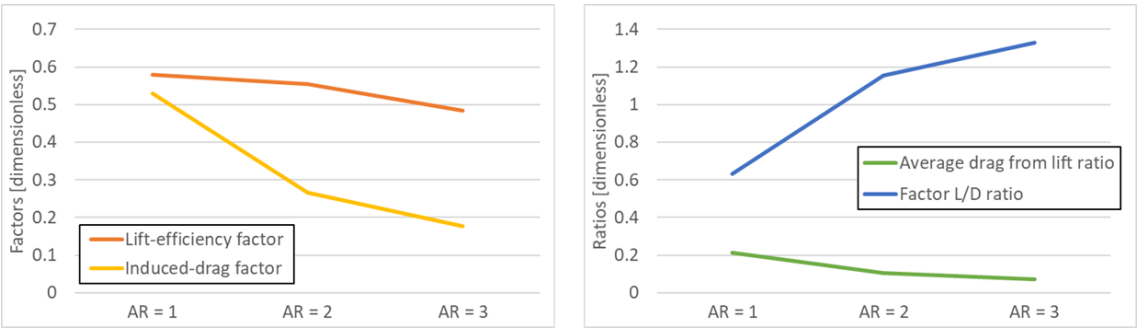

Source: Author.

The results shown on the left side of Figure 8 demonstrate that the aerodynamic performance follows inverse trends: both the lift-efficiency factor and the induced-drag factor peak at $AR = 1$. At that configuration, the lift-efficiency factor is equal to 57.85% and the induced-drag factor is equal to 53.05%. Increasing AR from 1 to 2 causes a reduction in lift-efficiency factor of 2.47% while reduces the induced-drag factor in half. On the other

hand, increasing AR from 2 to 3 causes a reduction in lift-efficiency factor of close to 6.9% while reducing only 33% of the remainder induced-drag factor. Likewise, the average drag from lift ratio follows almost the same proportions as the induced-drag factor. That decreasing advantage is shown through the factor L/D ratio which presents a steep increase of almost 90% with AR changing from 1 to 2 while only presenting a reduced gain of 14% with AR changing from 2 to 3.

Considering these values, the AR of the DPA is selected as 2. This allows the definition of the wing dimensions. The design-point from section 3.2 defined a span of 1 m. This defines a chord of 0.5 m considering a rectangular wing with AR equal 2. Such wing presents a total reference area $S_{ref} = 0.5\ m \cdot 1\ m = 0.5\ \text{m}^2 = 5000\ \text{cm}^2$.

4.5 Wing aerodynamic analysis

The aerodynamic qualities of the DPA's wing in fixed-wing flight are calculated using the aerodynamic coefficients of the STFP airfoil defined in section 4.3 and the aerodynamic factors from section 4.4. For the selected $AR = 2$, the lift-efficiency factor is estimated as 55.38% and the induced-drag factor as 26.52%. The lift results are presented on the left side of Figure 9 where the red line shows C_L and the blue line is C_l as already shown in Figure 7. On the other hand, the drag results are presented on the right side of Figure 9 where the blue line shows C_d, the red line shows C_{Di}, and the yellow line shows C_D.

Figure 9: *Wing lift (left) and drag (right) coefficients.*

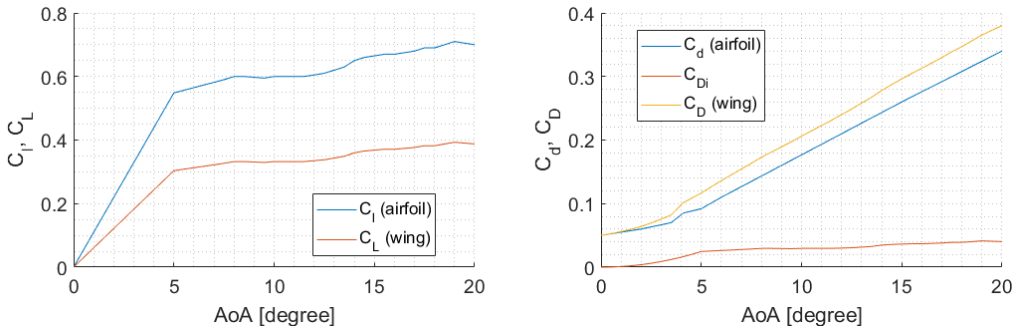

Source: Author.

A comparison with data from wind tunnel tests could be performed to ensure the theoretical results match the real aerodynamic performance of the wing. However, data from other authors is used instead because such a test is out of the scope of the present work. The works of (PELLETIER; MUELLER, 2000) and (ORTIZ; RIVAL; WOOD, 2015) provide aerodynamic coefficients for wings in the fixed-wing AoA range. These aerodynamic coefficients are equal or better than the ones calculated theoretically and presented in Figure 9. This validates the calculated aerodynamic coefficients with a conservative error level, since the aircraft will present an aerodynamic performance equal or better than the one estimated.

If AoA is different from zero, not all thrust (T_m) is available to provide horizontal acceleration as some part of it is on the vertical component. The horizontal thrust (T_h) is a function of the AoA and is defined as $T_h = T_m \cdot \cos(\alpha)$. As for each AoA, a different T_h is available and a different C_D is present, the maximum horizontal speed is a function of AoA, noted as $v_{max,\ D}$. Such speed is calculated considering the thrust of 1.1778 kgf

defined in section 4.2. These results are presented on the left side of Figure 10, where the blue line indicates T_h (almost constant) and the red line indicates $v_{max,\,D}$.

The minimum fixed-wing speed for level flight is calculated as 9.7993 m/s through the takeoff condition method proposed by (ROSA; TOPOROSKI, 2006). However, such speed is not the strict minimum speed as the C_L varies with each AoA. Considering this minimum flight speed and the maximum horizontal speed of $v_{max,\,D}$, the DPA's Re range is updated to between 2×10^5 and 9×10^5 which remains inside the UAV Re range discussed in section 4.3. These speeds as well as all aerodynamic forces are calculated considering the International Standard Atmosphere as defined by the ISO 2533:1975. The lift and drag forces considering $v_{max,\,D}$ are shown on the right side of Figure 10 where the blue line shows the lift, which peaks at 30 N, and the red line shows the drag, which is equal to the horizontal thrust on each AoA.

Figure 10: *T_h, $v_{max,\,D}$ (left), lift and drag (right) vs AoA.*

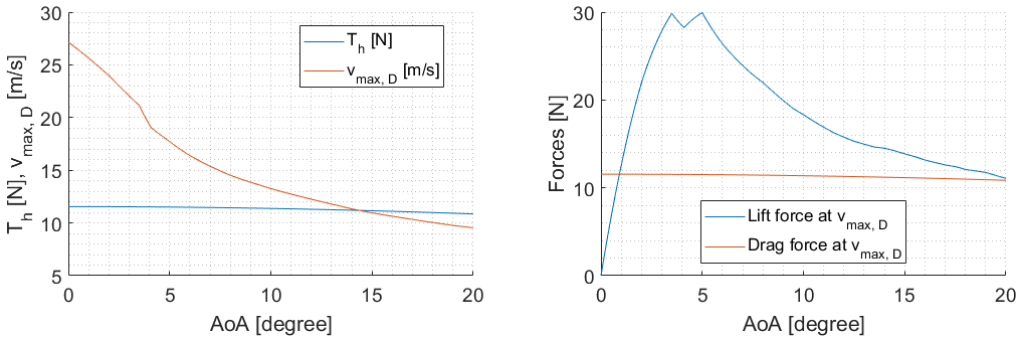

Source: Author.

During the fixed-wing flight, both the AoA or the horizontal speed can be increased to provide additional lift. As such, the maximum operational lift is defined as 1.359 kgf (or 13.33 N) configuring a lift excess of 150% of the MTOW. This value is selected to allow for some lift excess to be available for maneuvering. The produced lift is limited at all times to the maximum operational lift via limitation of flight speed. However, for any AoA smaller than 1.07° or larger than 15.79° the maximum horizontal speed is insufficient to produce the maximum operational lift. Thus, the limitation of speed is only active for AoA between 1.07° and 15.79°. This characterizes a speed regime, noted as $v_{max,\,L}$, which is shown on the left side of Figure 11 using a blue line.

Figure 11: *$v_{max,\,D}$, $v_{max,\,L}$ (left), lift and drag (right) vs AoA.*

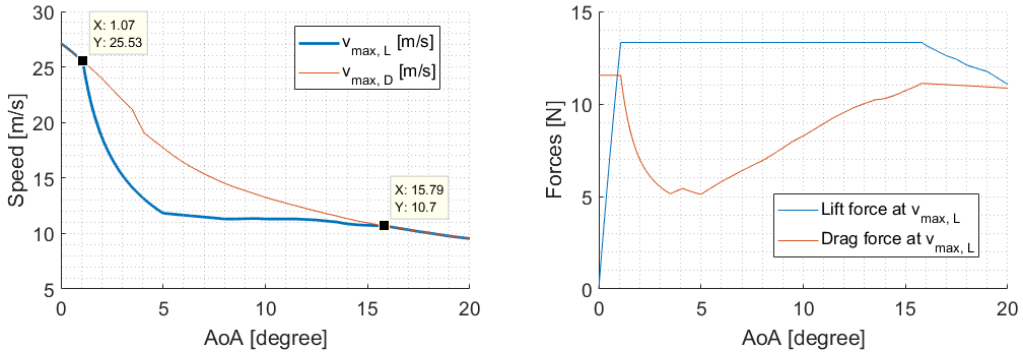

Source: Author.

The lift and drag forces considering $v_{max,\ L}$ are shown on the right side of Figure 11 where the blue line shows the lift and the red line shows the drag. In the figure, the conditions where the lift is limited at the maximum operational lift can be seen as the plateau of lift found at AoA between 1.07° and 15.79°. Inside this range, it is also possible to observe that the drag varies because the flight speed is smaller than the $v_{max,\ D}$ at each AoA value.

5 DETAILED DESIGN

This chapter presents the detailed design of the DPA. First, the material used in the wing is defined and tested. Due to the mission, the present work considers only a limited subset of the loads the work of (RAYMER, 1999) presents as typical for an aircraft. The aerodynamic load is studied in the structural analysis while the thrust load is considered during the powerplant detailed design. The landing load is studied during the tail detailed design whereas the maneuver load is analyzed during the aileron detailed design. In the sequence, the powerplant, ailerons, and tail are designed in detail and tested. In the end, the final detailed design is presented both as a body render and as a prototype.

5.1 Structures detailed design

The build-complexity is affected by the structural approach and the materials used. To streamline the build process, the present work uses a single-piece solid body without weight-reduction artifacts. The structure of most CEIM is composed of plastics, fiberglass, or carbon fiber while fixed-wing RC/AHC are usually built using lightweight wood, thermoplastics, or polystyrene foams as expanded polystyrene (EPS). The present work uses EPS sheet as the material to compose the aircraft body (and wing) because such material is inexpensive, highly available, and easy to work into the design. The selection of the thickness of the EPS sheet presents a trade-off since a larger cross section allows for more strength while also increasing weight.

The present work proposes a 2.5 cm thick EPS sheet as *candidate material* based on the author's experience. Such thickness defines a $t/c = 5\%$ configuring the wing's airfoil as an STFP airfoil. In the sequence, load tests are performed to validate the proposed thickness allows the wing to withstand the DPA's fixed-wing flight aerodynamic loads without additional reinforcements.

5.1.1 Testing aerodynamic loads

The present work tests the candidate material simulating the static aerodynamic load the lift causes in the structure during a fixed-wing flight. Such test is performed over the whole wing/body using surface load distributions because no spar and ribs are present in the DPA. These surface load distributions are composed of the product of the load percentages of spanwise and chordwise distributions. The maximum lift force determined in section 4.5 is equal to 1.3591 kgf while in section 4.2 the factor of safety and the load factor are defined as 1.25 and 1, respectively. This yields a lift test load of 1.6988 kgf which is equal to the integral of each surface distribution.

The work of (RAYMER, 1999) recommends two spanwise lift distributions to test aero-

dynamic loads. The *Schrenk's distribution* is used in most fixed-wing designs with nonelliptical wing while the *uniform-span distribution* is used due to the effects low-AR has on wingtip loading. The wingspan of 1 m is divided into 10 sections (or *stations*) of 10 cm span measured along the lateral axis (Y_C^P). For each station, a percentage of the test load is calculated through the surface of the station using both uniform-span and Schrenk's distributions. These results are presented in Figure 12.

Figure 12: *Spanwise distributions of lift load.*

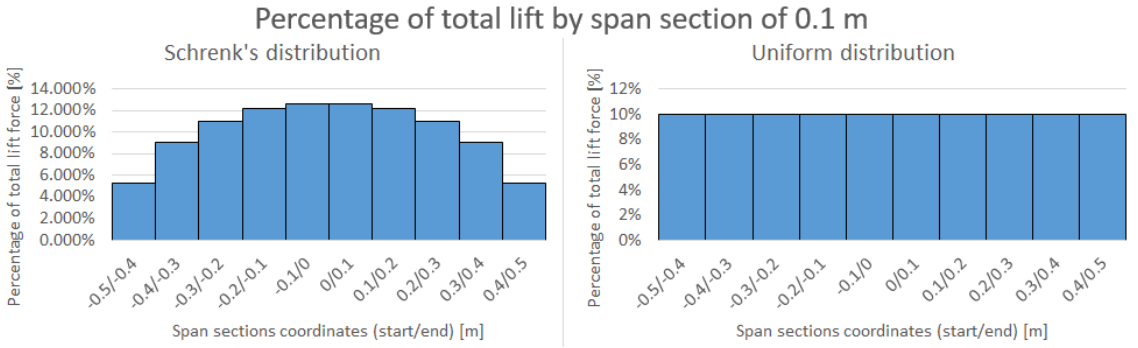

Source: Author.

Since the chordwise lift distribution is a function of the airfoil and its AoA, the present work uses data from (RAYMER, 1999) and (WINSLOW et al., 2017) to propose two distributions. The *uniform-chord distribution* is used for 0° of AoA while the *high AoA distribution* concentrates most of the load between LE and AC. The wing chord of 0.5 m is divided into 4 sections of 0.125 m measured from the LE. For each section, a percentage of the test load is calculated through the surface of the section using both uniform-chord and high AoA distributions. These results are presented in Figure 13.

Figure 13: *Chordwise distributions of lift load.*

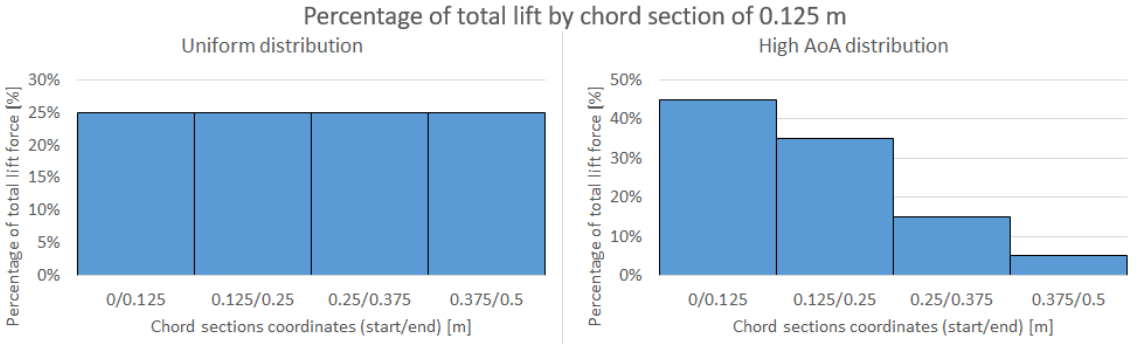

Source: Author.

The test body used in the aerodynamic load tests is a 2.5 cm thick EPS sheet measuring 1 m by 0.5 m without any reinforcements. The test body is fixed as a cantilever at half wingspan. And then, the top face of the projecting end is loaded with half of the four surface distributions (using sand inside plastic bags). The test setup is shown in Figure 14 where the blue arrows represent a generic distributed load and the red δ is the vertical deflection due to bending.

The expected results for the tests include: larger wingtip bending in the surface distributions composed with the uniform-span distribution if compared to Schrenk's; some

Figure 14: *Setup for aerodynamic load tests.*

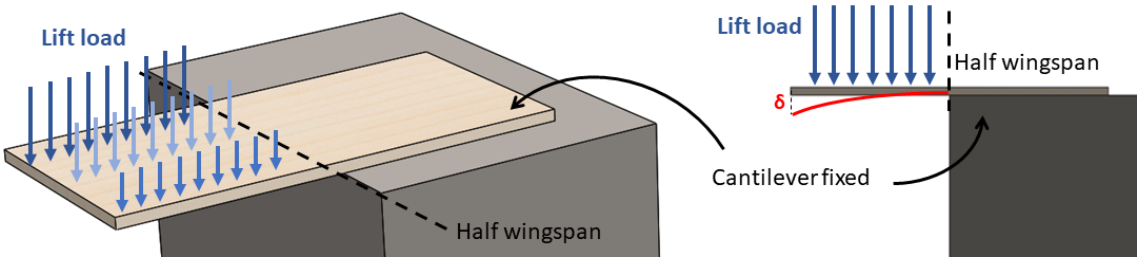

Source: Author.

wingtip torsion in the surface distributions composed with the high AoA distribution; no inelastic bending; and no structural failure.

The wingtip deflection in the unloaded scenario where only the test body's distributed weight is present is equal to $\delta_1 = 2\ cm$ which is 4% of the half span. The surface distribution composed from uniform-chord and Schrenk presents a $\delta_2 = 9\ cm$ (18% of the half span). The surface distribution composed from uniform-span and uniform-chord presents a $\delta_3 = 11\ cm$ (22% of the half span). When loaded with the surface distribution composed from uniform-span and high AoA, the LE presented a bending of 15 cm (30%) while the TE presented a bending of 10 cm (20%) with an almost linear deflection between both edges. This result indicates a small torsion (10%) is present on the wing in this case.

The tests showed the expected results. Thus, the candidate material is considered capable of withstanding the design loads. Hence, reinforcements are not required and no thinner EPS sheets are tested.

5.2 Powerplant detailed design

The DPA uses two outrunner brushless electric motors to provide the preliminary thrust defined in section 4.2. This type of motor operates as an asynchronous induction machine and is used in RC/AHC and CEIM paired with an electronic speed controller (ESC). The selected motor is a 28-26-1000kV model from NTM weighing 0.054 kgf and presenting a maximum rotation of 11,100 RPM (rotation per minute) with no load at 11.1 V. Each motor is paired to a Multistar 30A BLHeli multicopter-type ESC from Turnigy weighing 0.035 kgf and rated for constant current of 30 A. The motor's manufacturer recommends a dual-blade 9x4.7 inch fixed pitch propeller to provide 0.632 kgf of static thrust with a constant current of 10.2 A and peak of 15.85 A when operating at 11.1 V. Thus, the powerplant total current is 20.4 A constant and 31.7 A peak. The selected configuration is compatible with the DPA's battery, which is rated for 55.0 A constant current draw. This setup provides a total thrust of 1.264 kgf which is 0.0862 kgf (7.3187%) more than the preliminary thrust, yielding a detailed T/W of $1264/906 = 1.39$. This excess thrust allows for a completely built prototype to weigh even 0.972 kgf while still maintaining the preliminary T/W ratio of 1.3. To avoid a different from zero resultant rolling moment in fixed-wing flight (or an yawing moment in rotary-wing flight), the motors are configured to rotate in opposite directions, as recommended by (GUNDLACH, 2012).

A connector is required to support the motor in the LE wingtip. The present work proposes a structural connector composed of 3 pieces assembled in U profile through slots in the frontal plate and glued using cyanoacrylate and polyvinyl acetate (PVA). Such

setup is used instead of a frontal plate on deflection to reduce build-complexity. The motor is fixed to the connector using a cross-shaped manufacturer-provided motor mount. Then, the lateral pieces are fixed to each side of the EPS sheet using the same glues as the connector. The propeller, motor, motor mount, and structural connector are shown in Figure 15 where the full assembly of a half powerplant is presented.

Figure 15: *Exploded view of a half powerplant.*

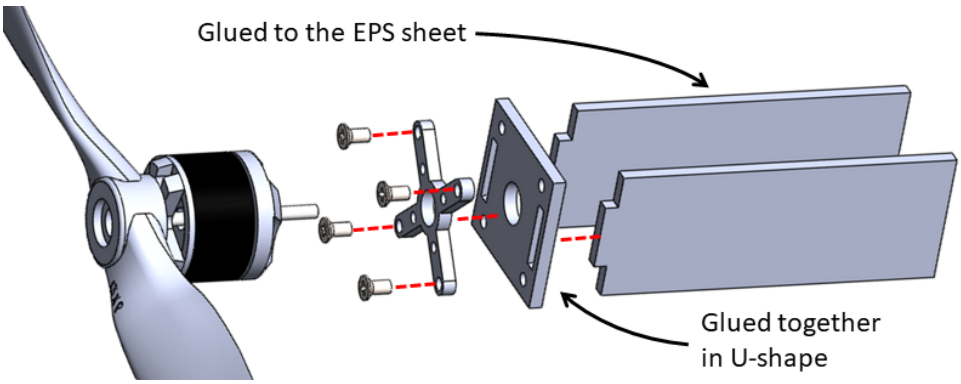

Source: Author.

The present work proposes a 3 mm thick polymethyl methacrylate (PMMA) sheet as *candidate material* for the connector based on the author's experience. In the sequence, load tests are performed to validate the candidate material, the design of the connector pieces, the assembly of the connector, and the fixation of the connector on the EPS sheet. The load test also indicates that the selected EPS sheet withstands without reinforcements the load created by the thrust's lever arm around the CG.

5.2.1 Testing thrust loads

The test body used in the thrust load tests is a 2.5 cm thick EPS sheet measuring 1 m by 0.5 m with a half powerplant installed at the LE wingtip. The test is performed with the test body fixed over its LE as a cantilever at half wingspan with the load fixed in the motor axis at the propeller mount. The setup is illustrated in Figure 16 where the green arrow represents a generic load.

Figure 16: *Setup for thrust load tests.*

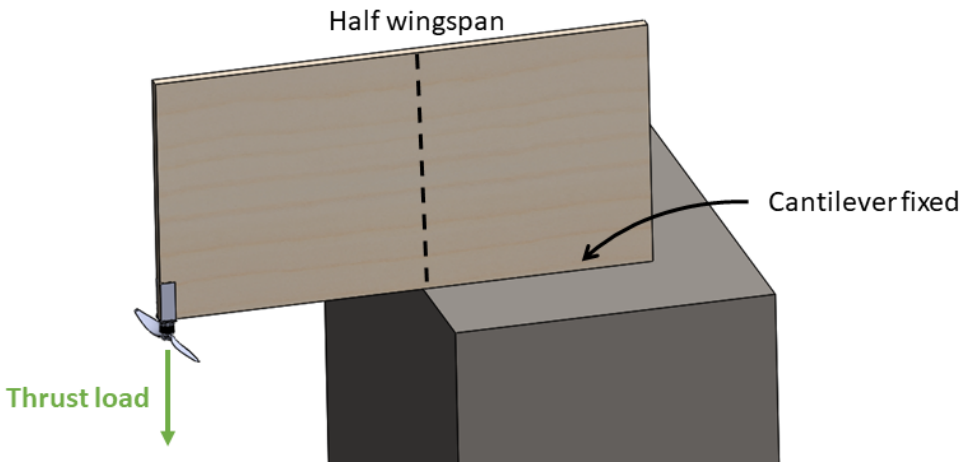

Source: Author.

The present work proposes a set of loads to simulate the static condition and dynamic maneuvers. Each motor produces half of MTOW as thrust when hovering in equilibrium. Thus, the first static load is equal to $0.906/2 = 0.453\ kgf$. The load of each motor is at most the maximum thrust during maneuvers. Thus, the second static load is equal to 0.632 kgf. Finally, the third static load is the maximum thrust with the 1.25 safety factor defined in section 4.2 which totals as $0.632 \cdot 1.25 = 0.790\ kgf$. The dynamic load is tested by installing the propeller and executing an acceleration from zero RPM to maximum RPM (and thus maximum thrust).

The expected results for the tests include: no bending along the LE; structural connector remaining assembled and fixed in the EPS sheet; no vibration during dynamic load test; and no structural failure. After testing, the actual results of the tests match these expectations. Thus, the candidate material, the structural connector, and the fixation on the wing are considered capable of withstanding the design loads.

5.3 Ailerons detailed design

The ailerons of the DPA are sized following guidelines presented in (DIEHL, 1923), (RAYMER, 1999) and (SADRAEY, 2012). However, the DPA's design considers some oversizing to compensate for the flying-wing design where a reduced number of control surfaces is present and these are required to act along various attitude axes. In addition, the oversizing also benefits the rotary-wing mode where larger ailerons provide more control authority.

The values presented by the three authors converge to a ratio between the aileron chord and the wing chord close to 30% if a small section of the span is used by the ailerons. Thus, the DPA's ailerons are rectangular with a 0.15 m chord and 0.2 m of span each. The resulting ailerons present an 81% efficiency (for chord and span) considering the metrics presented by (DIEHL, 1923). For any fixed-wing design, the maximum aileron deflection is limited by flow separation. The present work uses the typical limits of $\pm 30°$ during fixed-wing flight as recommended by (DIEHL, 1923) and (SADRAEY, 2012). However, the mechanical setup allows for deflection of $\pm 90°$ which is used by the rotary-wing mode.

The aileron (the moving control surface) is a single-piece body made of 2.5 cm thick EPS sheet. It presents a plain TE the same way as the wing. In the aileron station the wing also presents a plain TE. The aileron has a rounded LE together with a clearance of 0.5 cm to allow movement without interference. The lateral view of the aileron is shown on the right side of Figure 17.

According to (RAYMER, 1999), *flutter* is rapid oscillation of control surfaces caused by the air loads. To address flutter, the DPA uses ailerons with an overhang balance. Due to this, the rotation axis of the aileron is selected at its quarter-chord which is at 3.75 cm from the aileron LE. Additional 0.5 cm of clearance is added at the aileron TE to avoid interference with the wing TE plane at deflections smaller than 6.34° due to the aileron thickness. All the aileron-related clearances are removed from the wing. This defines the final dimension of the cutoff in the wing for each aileron as 16 cm of chord and 20 cm of span.

The DPA presents a wingspan region between the aileron outer edge and the wingtip because the aileron can not be placed exactly at the wingtip (as defined in section 3.2). The cross-section of the region defines its strength to loads. The present work proposes a *candidate cross-section* taking 5 cm of the wingspan based on the author's experience.

Load tests are performed to validate that the candidate cross-section and the proposed aileron assembly withstand the aileron load. The placement of the cutoffs for the aileron in the wing is shown on the left side of Figure 17.

Figure 17: *Body's top view (left) and aileron's lateral view (right).*

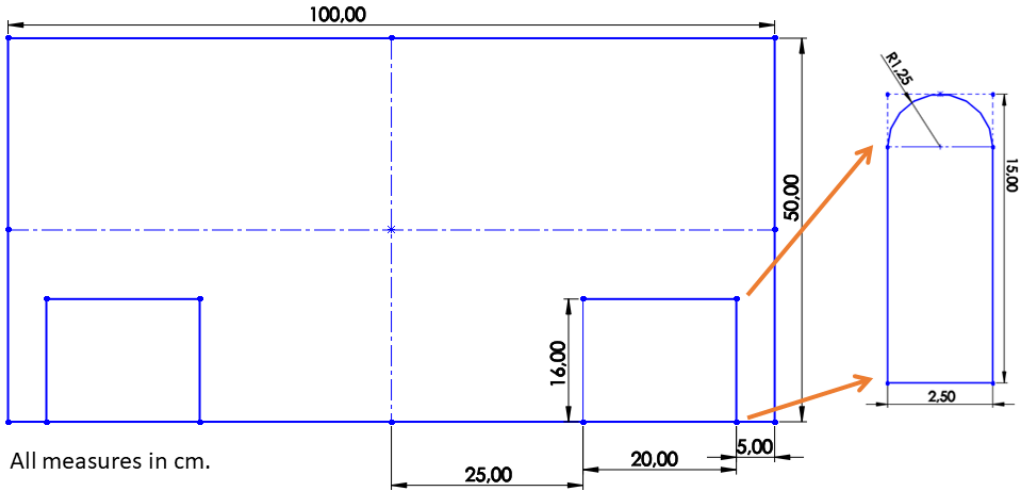

Source: Author.

The DPA uses an electric servomotor installed inside the wing driving the aileron rotation axis directly instead of the four-bar linkage used in most fixed-wing RC/AHC. This setup uses a slot in the top face of the wing at the inner edge of the aileron. A PMMA hardpoint is fixed inside the slot with cyanoacrylate and PVA. The servomotor is placed in the slot and screwed to the hardpoint, and then the slot is covered by an EPS lid. The selected servomotor is a 9g-type from Hextronik model HXT900 that weighs 0.0091 kgf with cables and presents 1.6 kgf-cm of torque when powered by RC/AHC standard voltage.

A PMMA hardpoint is installed on each side of the aileron moving piece (the control surface itself). The inner edge hardpoint has two holes to connect to the servomotor horn using screws while the outer edge hardpoint is fitted with a nut. The assembly of the active side of the axis is presented on the left side of Figure 18 where the servomotor is depicted in blue with its horn already installed (in white), the servomotor hardpoint is shown in gray, and the aileron inner edge hardpoint in dark brown. The passive side of the aileron axis uses a pillow-block structure made of PMMA with a central hole fitted with a nut at the rotation axis. A bolt installed from the wingtip connects this nut with the one from the outer edge aileron hardpoint, creating the rotation axis in the passive side. The full assembly is shown on the right side of Figure 18 where the aileron moving piece is depicted in transparent light green. In the figure, the hardpoints are visible in the same brown color: the two installed on the aileron and the one acting as pillow-block. The axis screw is visible is depicted in gray on the passive side.

5.3.1 Testing aileron loads

The present work uses the aerodynamic load to estimate the aileron load. The aileron deflection creates an additional lift on the station where the aileron is located. Such lift is observed in the aileron as a load over the aileron rotation axis and a distributed lift load over the moving control surface (RAYMER, 1999). Considering the fixed-wing mode, a load of 0.116 kgf (13.63% of the lift test load from section 5.1) is present over each

Figure 18: *Active side of axis (left) and full aileron assembly (right).*

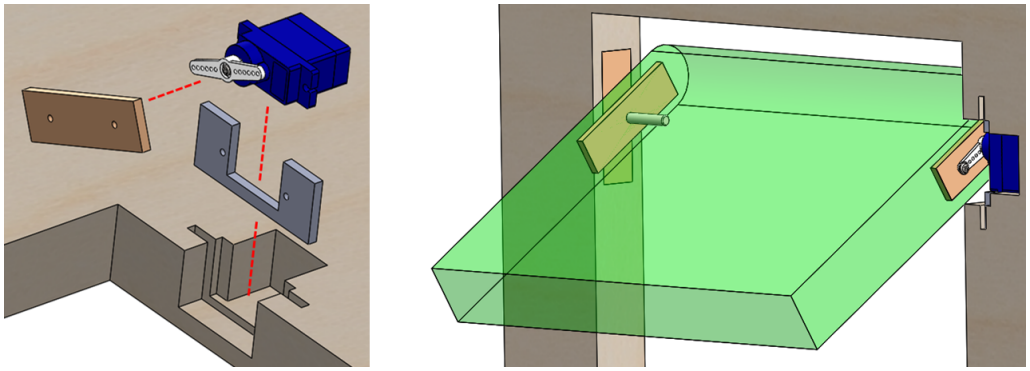

Source: Author.

aileron due to the ratio between aileron area and wing area and the aileron's efficiency. In contrast, the estimated load considering the rotary-wing mode is 1/3 of the MTOW for each aileron which is 0.302 kgf.

The test body used in the aileron load tests is a 2.5 cm thick EPS sheet measuring 1 m by 0.5 m with an aileron assembly installed. The test body is fixed as a cantilever at half span in a setup similar to Figure 14 allowing for the aileron periphery to be projected outside the horizontal support.

The present work proposes various setups to simulate the static condition and dynamic maneuvers using the larger 0.302 kgf test load. The static setup places the test load on the rotation axis at the top side of the aileron. This setup ensures the rotation axis and the cross-section withstand the load. The first dynamic setup is identical to the static setup except that the servomotor moves the full 180° range. This setup ensures the resistance is not dependent on the static condition. The second dynamic setup places a concentrated load ($0.302 \cdot (1/2) \cdot (2/3) = 0.101\ kgf$) at the aileron TE to simulate the distributed aileron load with the servomotor moving the full 180° range. This setup ensures the servomotor can provide torque to the maximum load condition and that the assembly withstands such condition. The third dynamic setup places a concentrated load ($1.6/11.25 = 0.143\ kgf$) in the aileron TE to simulate the maximum servomotor torque. This setup ensures the aileron assembly can operate at maneuver loads that require the maximum servomotor torque. Such load is equal to 0.429 kgf which is 47.35% of the MTOW and is larger than the 0.302 kgf proposed load.

The expected results for the tests include: no bending in the cross-section; aileron assembly remaining functional; servomotor operating in the maximum documented torque; no vibration during dynamic load test; and no structural failure. After testing, the actual results of the tests match these expectations. Thus, the candidate cross-section and the proposed aileron assembly are considered capable of withstanding the design loads.

5.4 Tail detailed design

The tail is designed to support the landed aircraft while also serving as a vertical stabilizer. Its dimension must withstand the landed/landing loads while presenting a small reference area to avoid an excessive increase in total aircraft drag in fixed-wing flight. The AR trade-off discussed for the wing in section 4.4 also applies to the tail. As such the present work aims at a tail AR equal to 2. For each tail body, a span of 15 cm is selected as the upper limit for sizing without spanwise reinforcements while being able to provide

stability for the landed aircraft (the size is 30% of the wing chord). A root chord of 15 cm and a tip chord of 0 cm are used to define an AR of 2 which is considered medium-high in tail sizing as discussed by (RAYMER, 1999).

Each tail body is a single-piece made of 2.5 cm thick EPS sheet using the same STFP airfoil as the wing and defining a tail t/c equal to 33%. Such bodies are installed aligned to the wing TE at midspan and fixed using cyanoacrylate and PVA. The tail assembly is shown in lateral view on the left side of Figure 19 while a 3D view is provided on the right side. In the sequence, load tests are performed to validate the proposed tail assembly.

Figure 19: *Tail assembly.*

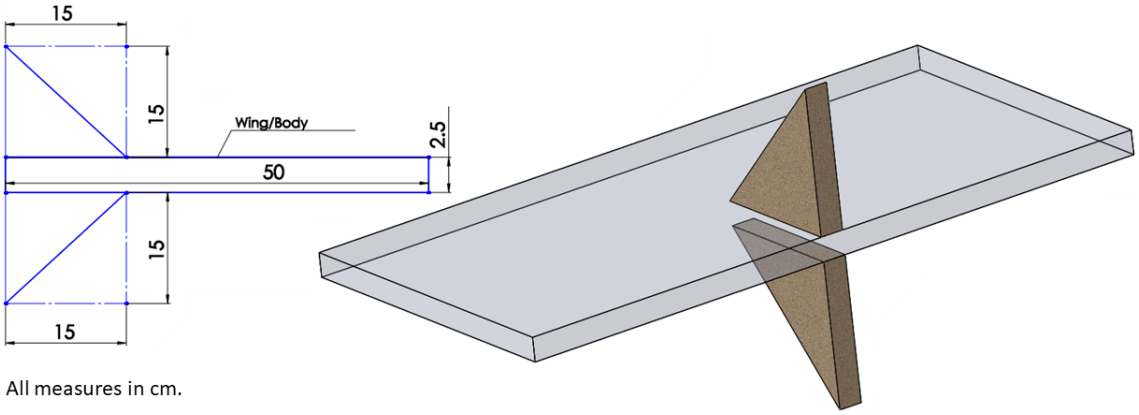

Source: Author.

5.4.1 Testing tail loads

The present work proposes various setups to simulate loads from static landed condition and landing maneuver. The most relevant load is the shear load in the connection between the tail and the wing considering that no transverse load is present since the landed aircraft is perpendicular to the ground. Dynamic loads from landings with roll or pitch angle different than zero ("one wheel landing") or with different than zero lateral speed ("crabbed landing") are out of the scope of the present work.

The test body used in the tail load tests is a 2.5 cm thick EPS sheet measuring 1 m by 0.5 m with a tail assembly installed. The first static setup places the test body in landed position. This setup ensures the tail can equilibrate the aircraft. The second static setup is identical to the first one, except that a concentrated load equal to the preliminary MTOW placed in the wing LE. This setup ensures the static equilibrium is kept with MTOW. The dynamic setup drops the aircraft loaded with MTOW in the wing LE from 0.5 m (equivalent to a chord) at zero pitch, yaw, and roll angles. This setup ensures the tail withstands a landing with thrust nulled early.

The expected results for the tests include: no bending in the tail bodies; tail assembly remaining connected to the EPS sheet; and no structural failure. After testing, the actual results of the tests match these expectations. Thus, the proposed tail assembly is considered capable of withstanding the design loads.

5.5 CG range

As established in section 4.1, the preliminary MTOW is composed of empty-weight and battery weight. The empty-weight of the DPA is divided in *operational empty-weight* and *avionics*. As defined by (RAYMER, 1999), avionics include all aviation electronics

from radios and sensors to flight control computers. In the case of the DPA, the avionics are not defined in the aeronautical design. However, avionics weight is estimated as equal to battery weight as a means to evaluate the CG of the aircraft.

The longitudinal stability of a flying-wing is defined by the CG range (RAYMER, 1999). As such, for a rectangular planar wing as the DPA, the CG must be restricted between the LE and the AC. Thus, the DPA uses a payload bay placed over the required CG range, allowing for variable placement of the battery and the avionics. Moreover, the payload bay is positioned at midspan to ensure a left-right symmetric CG.

The payload bay should create the minimum change possible in the wing thickness to avoid variation of aerodynamic qualities of the wing while withstanding the weight of the internal components. Considering the size of the battery, the payload bay is composed of a pre-built EPS box with internal dimensions of 11x13x3.5 cm, 0.5 cm-thick walls, and a removable lid. To install the box, a cutoff in the LE region of the mid wingspan is created in the wing with the dimensions of 12 cm in width (in span direction) and 14 cm in length (measured from the LE). The dimensions and placement are shown on the right side of Figure 20. The payload bay box with a total 4.5 cm height is placed with its floor aligned with the bottom face of the wing. This makes the additional 2 cm of thickness to be placed on only one side of the wing and visually defines the top face of the aircraft. This is shown on the left side of Figure 20.

Figure 20: *Top and lateral view of the aircraft body.*

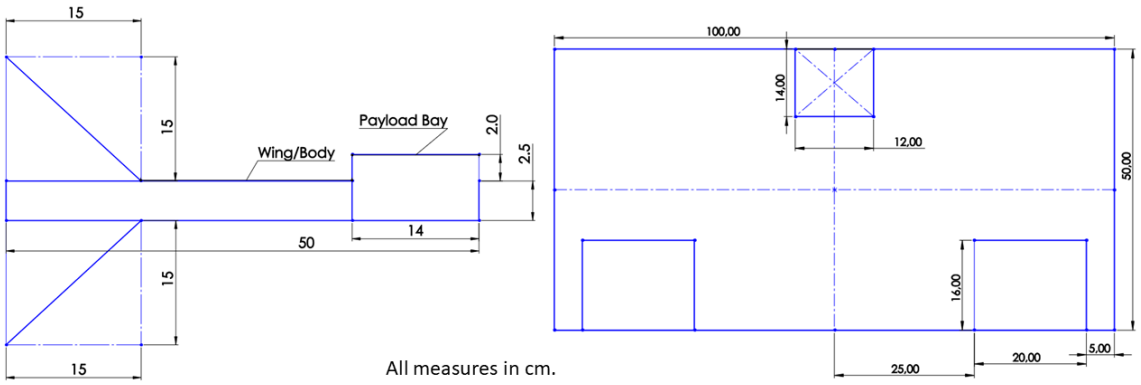

Source: Author.

The longitudinal CG of the DPA is estimated considering the operational empty-weight including powerplant, ESC, aileron, servomotor, tail, payload bay, various hard-points, and smaller components used in the assemblies as bolts and screws. The resulting CG is theoretically located at 9.98 cm from the LE at the midspan, which is inside the required CG range (the payload bay). However, the actual value is a function of fixation components as glue and tape which are distributed in the aircraft body and are dependent on the build process.

5.6 Build conclusion

The connection of the servomotor and ESC to the avionics in the payload bay is performed using RC/AHC standard cables. Such cables are routed through sulci in the wing and then are covered by a thick tape to return the wing surface to its original external flatness. This aims to limit the impact made on the aerodynamic qualities of the wing.

The final detailed design of the DPA is shown in Figure 21. In the figure, the wing is depicted in a light brown color with a group of sulci for cabling, the ESCs are shown as green bodies placed in the LE close to each motor, the ailerons are depicted as rectangular light brown pieces, and the payload bay and the tail are represented in gray at mid-wingspan at LE and TE, respectively. Besides these, the powerplant is visible on the LE wingtips and the servomotors are visible in blue close to the ailerons.

Figure 21: *Final detailed design (body render).*

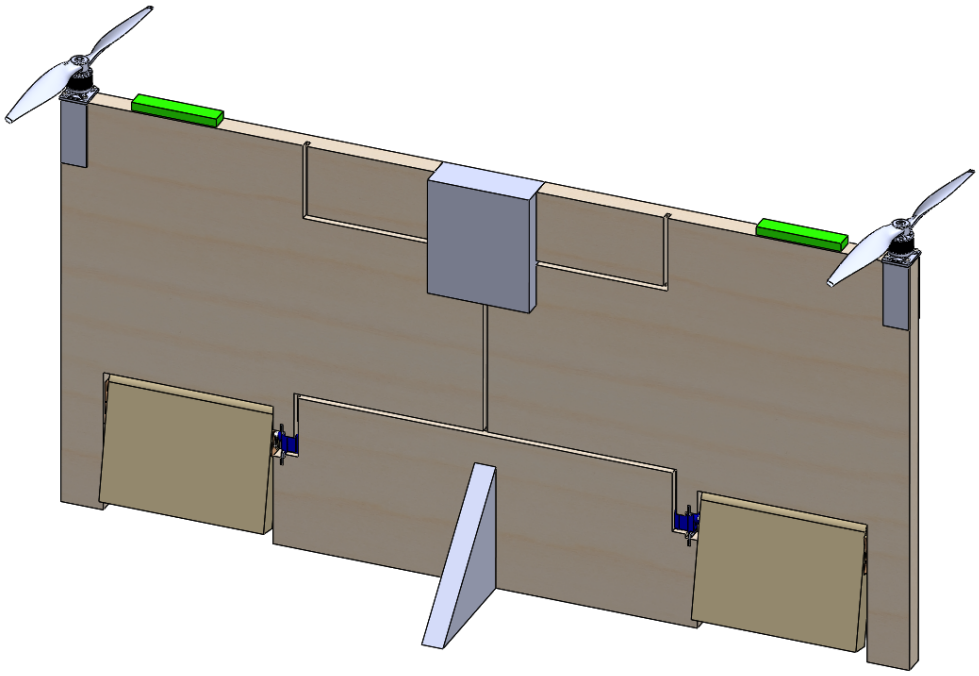

Source: Author.

A prototype is built following the aeronautical design. A new and clean 2.5 cm thick EPS sheet measuring 1 m by 0.5 m and weighing 0.095 kgf is used as the wing/body. Following the method established during the load tests, each component is installed then tested in the following order: tail, ailerons, and powerplant. In the sequence, payload bay and cabling are added. Moreover, the weight of the components and the total weight of the prototype is measured at each build step to estimate the fixation components (glue and tape) contribution. The resulting prototype DPA is shown in Figure 22.

The operational empty-weight of the prototype DPA is measured as 0.490 kgf. Considering the placement of the components and the variation of measured weight at each build step, the longitudinal CG of the prototype DPA is estimated as 10.57 cm from the LE which is inside the required CG range (the payload bay). To validate the proposed CG, the prototype is placed over a thin test axis parallel to the lateral axis (Y_C^P) and left to rotate in pitch. When the test axis is placed on the CG, the equilibrium condition in pitch is obtained. Such a test showed that the longitudinal CG for the built prototype is found between 10 and 11 cm from the LE. The same is tested in the longitudinal direction (parallel to the vertical axis Z_C^P) to ensure the prototype is left-right symmetric and the lateral CG is at the midspan.

Considering an additional weight of 0.326 kgf (battery plus avionics) placed inside the payload bay, the CG range as a function of such weight is calculated. The results are

Figure 22: *Final detailed design (prototype picture).*

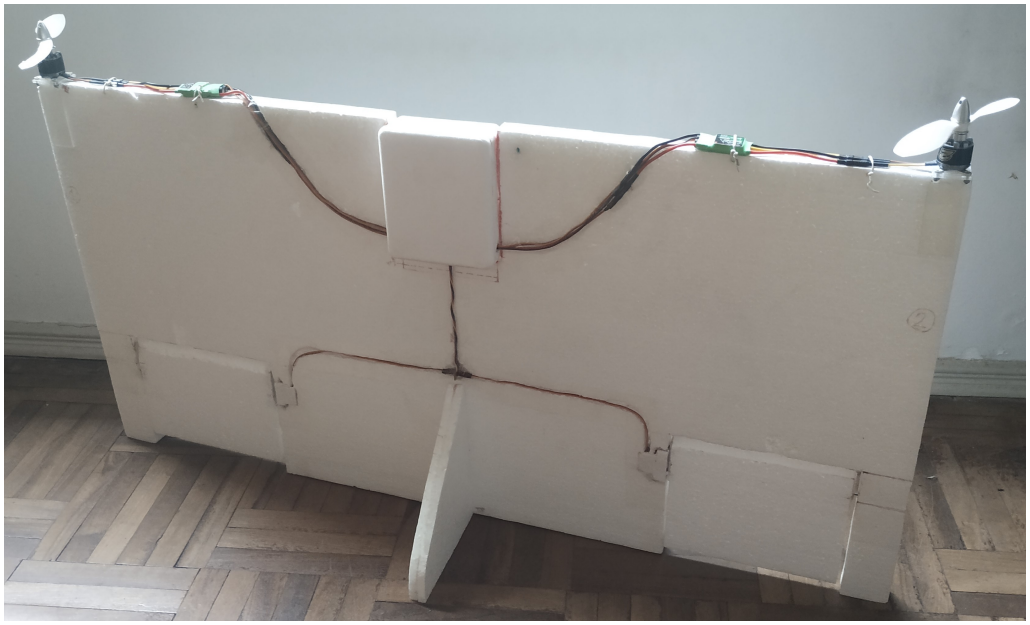

Source: Author.

presented in Figure 23 showing the CG is inside the required range (the payload bay) for all conditions.

Figure 23: *CG placement range.*

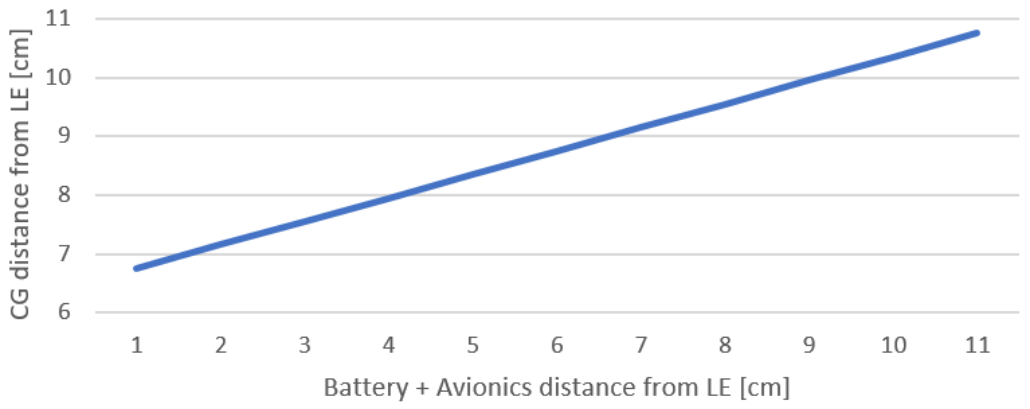

Source: Author.

The DPA's empty-weight from section 4.1 is estimated as 0.743 kgf. In the case of the built prototype, an extra 0.253 kgf is available to the avionics. Even considering the estimation of avionics weighing equal to the battery (0.163 kgf), a remainder of 0.090 kgf is still available. Such weight allows, for example, the addition of reinforcements weighting almost the equivalent of an additional 2.5 cm thick EPS sheet.

Considering the built prototype, the final weights are summarized in: operational empty-weight of 0.490 kgf; estimated avionics weight of 0.163 kgf; empty-weight of 0.653 kgf; battery weight of 0.163 kgf; MTOW of of 0.816 kgf. These values configure an EWF of 80% and a T/W of 1.549.

6 RESULTS AND DISCUSSION

This chapter summarizes the results of the aeronautical design and links them to the specific objectives defined in chapter 1. The conceptual phase defined a mission for the DPA answering to the specific objective (i). Other than the mission, the main result of the conceptual design is the aircraft concept itself. However, the conceptual trade-offs discussed also compose results in terms of CUAV-VTOL aeronautical design. In contrast, the preliminary and detailed phases present more explicit results. Such results are discussed in the two following sections and they answer to the specific objectives (ii) and (iii).

6.1 Preliminary Design

The wing was studied in section 4.4. The components of wing performance relevant to the flight conditions defined in the mission were analyzed. Based on this, two metrics were established which can be used to compare simultaneously the performance of lift and drag of wings with different AR. Considering build-simplicity and aerodynamic conditions, a preliminary AR range was established. Using the defined metrics, the wing performance inside the AR range was estimated and analyzed yielding the DPA's selected AR.

The airfoil was defined as STFP in section 3.2 aiming to simplify the build. Such airfoil was studied in section 4.3. The theoretical performance of the STFP airfoil was analyzed resulting in the conclusion that the selected airfoil presents performance similar to conventional airfoils in the flight conditions of the mission. Then, test data from various works were combined to compose the aerodynamic coefficients of the STFP airfoil resulting in a full detailed AoA range (0 to 90°).

Combining the results from section 4.4 and section 4.3, the wing performance for the DPA was estimated in section 4.5. The calculated performance was compared to test data from various works to evaluate the obtained results. This yielded the conclusion that the proposed wing aerodynamic coefficients of the DPA were correct with a conservative level of error. Thus, indicating that the aircraft will present an aerodynamic performance equal or better than the one estimated.

Still in section 4.5, the flight conditions were studied resulting in a speed regime including minimum speed for level flight and maximum speed as a function of drag forces and maximum operational lift. Estimated aerodynamic forces also indicate that the designed wing enables fixed-wing flight with remaining excess performance.

6.2 Detailed Design

The detailed design includes the design of the components as well as its validation through tests and the design of its building process. Thus, the specific results of the detailed phase are the components designed in detail, validated, and built.

In section 5.1 the wing material was selected to configure an STFP airfoil. The expected distributed loads of fixed-wing flight were estimated. The designed wing was built and tested. This resulted in the validation of the material and the wing design.

The DPA's motors were selected in section 5.2. The structural connector for the powerplant and the related fixations were designed in detail including its fabrication. In section 5.3 the ailerons were sized and their placement in the wing was defined. The structural components (supports, axis, and connectors) were designed in detail including its assembly. The expected loads for both components were estimated considering dynamic maneuvers. The designed components were built and tested. This resulted in the validation of the components and their fixation design.

In section 5.4 the tail was sized, its material was selected and its fixation was designed. The expected landing/landed loads were estimated. The designed tail was built and tested validating the component design and its fixation. The payload bay of the aircraft was designed in section 5.5. Considering the weight of the designed components, the aircraft CG was calculated. The resulting location was inside the payload bay, which is the expected stability range as described in section 3.2 and section 5.5.

The aeronautical design was completed in section 5.6 answering to the specific objective (ii). Based on this, a prototype of the DPA was built. The designed validation tests were applied in each component as described in section 5.6 validating the build and answering to the specific objective (iii). The CG of the prototype was calculated as close to the designed value. The calculated CG was found via equilibrium condition in the calculated location in the prototype validating the expected stability range. The prototype built as per the aeronautical design is the main result of the detailed design.

A highlight related to the design-point and sizing results is also due. In section 3.2 the design-point was defined as close to 1 kgf. The results from the sizing in section 4.1 matched the selected design-point defining an MTOW of 0.906 kgf. In addition, the results from the build presented in section 5.6 showed an actual MTOW of 0.816 kgf. These results validate the selected design-point and sizing estimations.

7 CONCLUSION

This work presented the aeronautical design process of a CUAV-VATOL aircraft, intended as a development platform aircraft (DPA) which will serve, in future works, as a tool for the development of flight control systems. It comprised the three typical phases of aircraft design including: conceptual analysis, based on the UAV characteristics and the effects present in a convertible aircraft; aerodynamic analysis of the fixed-wing flight, accompanied by the propulsion system to enable both flight modes; and detailed design of all the aircraft components. The whole design was carried out considering its mission as a development platform, implying that the design choices (mainly the conceptual ones) aim to facilitate the subsequent control systems study and development.

As such, the main contributions of this work comprise a functional aircraft platform for the development of control systems and the related research and development in CUAV aircraft design. Finally, the design, its prototype, and the reported flight are the main results of this work.

In conclusion, this work achieved a credible CUAV-VATOL aircraft design. Such aircraft presents acceptable performance and flight characteristics and it is capable of fulfilling its objective as a development platform for flight control systems.

7.1 Link to future works

The complete aeronautical design and the built prototype allow for future works to utilize the DPA as a development platform as intended by the author and described in chapter 1. To establish a stability augmentation system and a flight control system for the DPA, a mathematical model of the aircraft dynamics is required. Such modeling was performed and the results are presented in Appendix B. To partially validate the model and to analyze some of the proposed simplification hypotheses, the maiden flight of the prototype was performed in open-loop with manual controls. The results of such flight and its implications on the control systems design are also detailed in Appendix C.

On the present stage of development, the DPA can now be used as a platform to develop stability augmentation algorithms and flight control systems. The future works may include, but are not restricted to:

- Establish the state estimation and control architectures;
- Design the embedded avionics (sensors, radios, and flight computer);
- Implement a stability augmentation system;
- Implement a flight control system;

REFERENCES

ANDERSON, J. D. *Fundamentals of Aerodynamics*. 3rd edition. New York: McGraw-Hill Science, 2001. ISBN 978-0-07-237335-6.

ANDERSON, J. D. *Introduction to Flight*. 8th edition. New York: McGraw-Hill Education, 2015. ISBN 978-0-07-802767-3.

BARTH, J. M. O. et al. Towards a Unified Model-Free Control Architecture for Tailsitter Micro Air Vehicles: Flight Simulation Analysis and Experimental Flights. In: AIAA Scitech 2020 Forum. [S.l.: s.n.], 2020.

BOEING. *Statistical Summary of Commercial Jet Airplane Accidents: Worldwide Operations | 1959 – 2017*. Seattle, Washington, USA, 2018. p. 14. Available from: <www.boeing.com/news/techissues/pdf/statsum.pdf>. Visited on: 31 Mar. 2021.

CHANA, W. F.; COLEMAN, J. F. S. *World's First VTOL Airplane Convair/Navy XFY-1 Pogo*. Warrendale, PA, Nov. 1996. Available from: <https://www.sae.org/publications/technical-papers/content/962288/>. Visited on: 1 Apr. 2021.

DIEHL, W. S. *Notes on the design of ailerons*. NACA Technical Notes. [S.l.], 1923.

ESCARENO, J. A. *Conception, modélisation et commande d'un drone convertible*. 2008. PhD Thesis – Université de Technologie de Compiègne, Compiègne.

FAGE, A.; JOHANSEN, F. C. On the Flow of Air behind an Inclined Flat Plate of Infinite Span. *Proceedings of the Royal Society of London. Series A, Containing Papers of a Mathematical and Physical Character*, v. 116, n. 773, p. 170–197, 1927. ISSN 09501207. Available from: <www.jstor.org/stable/94722>. Visited on: 4 Mar. 2021.

FLOREANO, D.; WOOD, R. J. Science, technology and the future of small autonomous drones. *Nature*, v. 521, p. 460–466, 2015. Available from: <http://infoscience.epfl.ch/record/208757>.

FRANK, A. et al. *Hover, Transition, and Level Flight Control Design for a Single-Propeller Indoor Airplane*. Massachusetts Institute of Technology, 2007.

GREEN, W. A fixed-wing aircraft for hovering in caves, tunnels, and buildings. In: 2006 American Control Conference. Minneapolis, Minnesota, USA: [s.n.], June 2006.

GREEN, W. A MAV that flies like an airplane and hovers like a helicopter. In: PROCEEDINGS of the 2005 IEEE/ASME International Conference on Advanced Intelligent Mechatronics. Monterey, California, USA: [s.n.], July 2005.

GUNDLACH, J. *Designing Unmanned Aircraft Systems: A Comprehensive Approach*. Manassas, Virginia: American Institute of Aeronautics and Astronautics, 2012. (AIAA education series). ISBN 978-1-60086-843-6.

ICAO. *Annex 7 - Aircraft Nationality & Registration Marks*. [S.l.], 1981. Available from: <https://store.icao.int/collections/annex-7-aircraft-nationality-and-registration-marks>. Visited on: 3 Feb. 2021.

ICAO. *Unmanned Aircraft Systems (UAS)*. Montréal, 2011. Available from: <https://www.icao.int/Meetings/UAS/Documents/Circular%20328_en.pdf>. Visited on: 3 Feb. 2021.

KNOEBEL, N. et al. Preliminary Modeling, Control, and Trajectory Design for Miniature Autonomous Tailsitters. In: AIAA Guidance, Navigation, and Control Conference and Exhibit. [S.l.]: American Institute of Aeronautics and Astronautics, 2006.

MCCORMICK, B. *Aerodynamics of V/STOL flight*. 1st edition. Pennsylvania: Academic Press, 1967. ISBN 978-0-486-40460-8.

MCCORMICK, B. *Aerodynamics, Aeronautics, and Flight Mechanics*. 2nd edition. Pennsylvania: Wiley, 1995. ISBN 978-0-471-11087-3.

NELSON, R. *Flight stability and automatic control*. 1st edition. [S.l.]: McGraw-Hill, 1989. ISBN 978-0-07-046218-2.

ORTIZ, X.; RIVAL, D.; WOOD, D. Forces and Moments on Flat Plates of Small Aspect Ratio with Application to PV Wind Loads and Small Wind Turbine Blades. *Energies*, v. 8, n. 4, 2015.

PELLETIER, A.; MUELLER, T. J. Low Reynolds Number Aerodynamics of Low-Aspect-Ratio, Thin/Flat/Cambered-Plate Wings. *Journal of Aircraft*, v. 37, n. 5, p. 825–832, Sept. 2000.

RAYMER, D. *Aircraft Design: A Conceptual Approach*. 3rd edition. Washington, DC: American Institute of Aeronautics and Astronautics, 1999. (AIAA education series). ISBN 978-1-56347-281-7.

ROSA, E. DA; TOPOROSKI, J. *Introdução ao projeto aeronáutico: uma contribuição à competição SAE Aerodesign*. Florianópolis: UFSC/GRANTE, 2006.

SADRAEY, M. *Aircraft Design: A Systems Engineering Approach*. [S.l.]: Wiley, 2012. (Aerospace Series). ISBN 978-1-118-35280-9.

SELIG, M. S.; DONOVAN, J. F.; FRASER, D. B. *Airfoils at low speeds*. [S.l.]: H.A. Stokely, 1989.

SELIG, M. S.; GUGLIELMO, J. J. High-Lift Low Reynolds Number Airfoil Design. *Journal of Aircraft*, v. 34, n. 1, p. 72–79, Jan. 1997.

SHELDAHL, R. E.; KLIMAS, P. C. *Aerodynamic characteristics of seven symmetrical airfoil sections through 180-degree angle of attack for use in aerodynamic analysis of vertical axis wind turbines*. [S.l.], 1981. Available from: <https://www.osti.gov/biblio/6548367/>. Visited on: 2 Feb. 2021.

SMEUR, E. J. J.; BRONZ, M.; CROON, G. C. H. E. DE. Incremental Control and Guidance of Hybrid Aircraft Applied to a Tailsitter Unmanned Air Vehicle. *Journal of Guidance, Control, and Dynamics*, v. 43, n. 2, p. 274–287, 2020.

STONE, R. H. Aerodynamic Modelling of a Wing-in-Slipstream Tail-Sitter UAV. In: 2002 Biennial International Powered Lift Conference and Exhibit. Williamsburg, Virginia: American Institute of Aeronautics and Astronautics, 2002a.

STONE, R. H. The T-Wing Tail-Sitter Research UAV. In: 2002 Biennial International Powered Lift Conference and Exhibit. Williamsburg, Virginia: American Institute of Aeronautics and Astronautics, 2002b.

USN. *2nd US Navy Centennial Newsletter*. [S.l.: s.n.], 2009. Available from: <https://www.public.navy.mil/airfor/centennial/Documents/2nd%20Centennial%20Newsletter.pdf>. Visited on: 31 Mar. 2021.

VERLING, S. et al. Full Attitude Control of a VTOL tailsitter UAV. In: 2016 IEEE International Conference on Robotics and Automation (ICRA). Stockholm, Sweden: [s.n.], May 2016.

WINSLOW, J. et al. Basic Understanding of Airfoil Characteristics at Low Reynolds Numbers (10e4–10e5). *Journal of Aircraft*, v. 55, n. 3, p. 1050–1061, Dec. 2017.

WOODS, R. J. Convertiplanes and Other VTOL Aircraft. In: SAE Technical Paper. Warrendale, PA: [s.n.], 1957.

APPENDIX A - REFERENCE FRAMES

This chapter presents the coordinate systems and conventions of directions that compose the reference frames used in the present work. Such frames are relevant to the attitude analysis of the aircraft during the design process and to the mathematical modeling.

The conventions for frames and orientations can vary largely (RAYMER, 1999). The typical frames used for stability and control analysis in fixed-wing aircraft are the inertial fixed frame and the body frame which translates and rotates with the airplane (NELSON, 1989).

The present work uses three frames with right-handed coordinate systems: inertial, body and pose. The main difference is that the body frame translates with the DPA while the pose frame rotates with the DPA around its CG. This setup allows for focus on the attitude of the DPA. These frames and the related measures are discussed in the following sections. The Figure 4 (repeated here as Figure 24 for convenience) shows the placement of the frames including the pose frame on a render of the DPA.

Figure 24: *Reference frames and measures (same as Figure 4).*

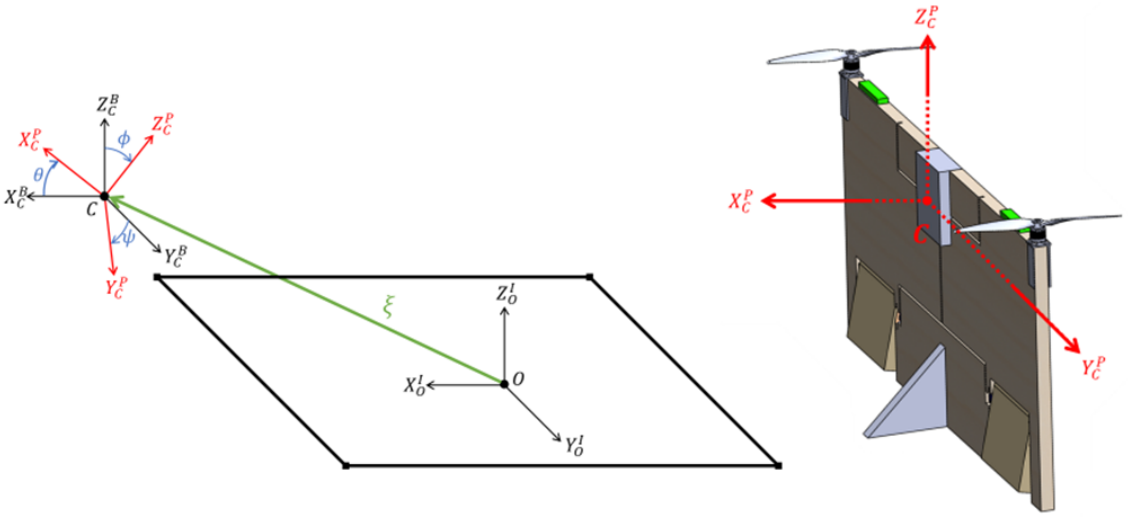

Source: Author.

The inertial frame (I) has its origin (O) located at the ground. This frame is associated with the coordinate axes system $\{X_O^I, Y_O^I, Z_O^I\}$. The body frame (B) has its origin (C) located at the CG and its coordinate axes system $\{X_C^B, Y_C^B, Z_C^B\}$ is in the same orientation as the inertial frame.

The position of the CG is measured between the inertial and body systems (from O to C) as a column of three elements measured along the system $\{X_O^I, Y_O^I, Z_O^I\}$ and noted by

the position vector:

$$\xi \doteq (x, y, z)^T \tag{5}$$

The pose frame (P) also has its origin (C) located at the CG. However, its coordinate axes system $\{X_C^P, Y_C^P, Z_C^P\}$ is fixed on the DPA structure and has the same orientation during both flight modes. The angular orientation of the aircraft (the attitude) is described by the three Euler angles: yaw (ψ), pitch (θ), and roll (ϕ). These three angles are measured, following right-hand convention, between the body and pose systems and they are components of the attitude vector:

$$\eta \doteq (\theta, \phi, \psi)^T \tag{6}$$

The pose frame has the Z_C^P axis pointing upwards while in rotary-wing flight. In contrast, the positive direction of the X_C^P axis points upwards while in fixed-wing flight while Z_C^P becomes the forward direction. It is important to highlight that the attitude angles are defined considering the rotary-wing mode over the fixed-wing.

The lateral axis (Y_C^P) passes through the DPA from left wingtip to right wingtip. A moment along this axis alters the pitch angle (θ) in both flight modes. The vertical axis (Z_C^P) passes through the DPA from TE to LE. A moment along this axis alters ψ. Such angle is the "rotary-wing yaw angle" as well as the "fixed-wing roll angle". The longitudinal axis (X_C^P) passes through the DPA from the bottom face to the top face. A moment along this axis alters ϕ. Such angle is the "rotary-wing roll angle" as well as the "fixed-wing yaw angle".

APPENDIX B - MATHEMATICAL MODELING

This chapter presents a mathematical model for the DPA. First, a set of simplification hypotheses are presented based on the mission. In the sequence, the attitude modeling is discussed considering both flight modes. In the end, the actuators (ailerons and power-plant) are discussed with their respective models.

The forces considered in this modeling are the lift L, drag D, aerodynamic pitching moment M_w, thrust from motors $T_k,\ k = 1,2$, and the aileron moments. The typical notation for fixed-wing aircraft is L, M, and N representing moments along the roll, pitch, and yaw axis, respectively (NELSON, 1989). Such notation is not used in the present work to avoid confusion from the transition between flight modes. Thus, the aileron moments are noted $M^i_{\delta_j}$ for $i = X,Y,Z$ referring to the pose frame axes, and $j = 1,2$ referring to the two ailerons. Even the pitch moment (around Y^P_C) is described with two separated aileron moments when the ailerons act in common mode. The aerodynamic forces are based on coefficients calculated in the aeronautical design and are summarized by the following equations:

$$\begin{cases} L = qS_{ref}C_L \\ D = qS_{ref}C_D \\ M_w = cqS_{ref}C_M \end{cases} \tag{7}$$

where $q = \frac{1}{2}\rho V^2$ is the dynamic pressure, ρ is the atmospheric density, V is the inertial speed calculated through 2-norm of $\dot{\xi}$, c is the DPA's wing chord, and C_M is the wing pitching-moment coefficient which is a constant in the DPA'case due to the STFP airfoil.

In terms of layout, the DPA's actuators are noted with subscript 1 for the right-side when seen from the TE and subscript 2 for the left side. In terms of geometry, the distance between the CG and the AC is noted l_{AC} measured along Z^P_C while the distance between the motor and the CG is noted l_m measured along Y^P_C.

B.1 Flight path simplifications

The DPA's thrust line is parallel to the Z^P_C axis. This implies that a horizontal speed is present if the non-horizontal angles are different than zero. This condition is evident for pitch (θ) in both flight modes and is summarized in the following relation:

$$\psi = 0 \begin{cases} \theta = 0 \iff \dot{x} = 0 \\ \phi = 0 \iff \dot{y} = 0 \end{cases} \tag{8}$$

The mission defined in section 3.1 implies that the following simplification hypotheses (or *assumptions*) are reasonable for the rotary-wing mode:

(I) All linear speeds (the components of $\dot{\xi}$) are small and tend to zero.

(II) Horizontal speeds are decoupled, i.e., $\dot{x} \cdot \dot{y} = 0$.

(III) Pitch and roll angles are decoupled, i.e., $\theta \cdot \phi = 0$.

(IV) Altitude is changed only from stable hover condition, i.e., $\dot{z} \neq 0 \implies \theta = \phi = \dot{\psi} = 0$.

(V) Yaw is changed only from stable hover condition, i.e., $\dot{\psi} \neq 0 \implies \theta = \phi = \dot{x} = \dot{y} = \dot{z} = 0$.

Assumption (IV) implies that no relative angle between the DPA and $\dot{\xi}$ is present in vertical maneuvers (kind of a "zenith AoA"). Thus, no aerodynamic force is present during changes of altitude from hover. In addition to this, assumption (I) implies that the aerodynamic forces, which are proportional to the square of the speed, are also small and tend to zero. The consequences of assumption (IV) already defined null aerodynamic forces over vertical movements. Forward movement (in direction of X_C^B if $\psi = 0$) presents zero lift and different from zero drag due to the high AoA present. In contrast, lateral movement (in direction of Y_C^B if $\psi = 0$) presents zero lift and drag due to low speed and thin wing. Considering assumptions (III) and (V), all three components of the attitude are decoupled, which defines an additional simplification hypothesis (VI). However, coupling between the vertical direction and each of the lateral and forward directions remains due to the DPA's thrust line.

The presented simplification hypotheses are similar to the ones from other CUAV modeling works as (KNOEBEL et al., 2006) and (ESCARENO, 2008). No additional simplification hypothesis is proposed for the fixed-wing mode other than the mission itself.

B.2 Attitude models

The present work proposes a single model for both flight modes based on the equations of fixed-wing flight presented by (RAYMER, 1999) and (NELSON, 1989) and on the equations and discussions related to CUAV flight presented by (STONE, 2002b), (KNOEBEL et al., 2006) and (ESCARENO, 2008). The proposed equations are derived from:

$$\sum \overrightarrow{\mathrm{M}_{\mathrm{C}}^{\mathrm{P}}} = I\ddot{\eta} \iff \begin{cases} \sum M_{X_C^P} = I_X \ddot{\phi} \\ \sum M_{Y_C^P} = I_Y \ddot{\theta} \\ \sum M_{Z_C^P} = I_Z \ddot{\psi} \end{cases} \tag{9}$$

where $\overrightarrow{\mathrm{M}_{\mathrm{C}}^{\mathrm{P}}}$ represents the moments around the pose frame, I is the inertia matrix, and the terms I_i for $i = X, Y, Z$ refer to principal moments of inertia around the pose frame axes.

As described by (RAYMER, 1999), the stability and control analysis of a left-right symmetrical fixed-wing aircraft can be decoupled into longitudinal and lateral-directional. Considering (VI), such decoupling is also possible for the rotary-wing flight of the DPA. In the present work, the longitudinal analysis is presented first because θ defines the flight mode and the lateral-direction equations are dependant on the flight mode.

B.2.1 Longitudinal analysis

The pitching-moment equation around the CG is defined based on the free-body diagram presented on the right side of Figure 25. To describe both flight modes, the proposed equation includes lift, drag and the wing aerodynamic moment:

$$\sum M_{Y_C^P} = M_w - l_{AC}(L\cos\alpha + D\sin\alpha) + M_{\delta_1}^Y + M_{\delta_2}^Y \tag{10}$$

The longitudinal stability and control are relevant topics for a flying-wing. Equation 10 is simplified to analyze the pitch static stability in fixed-wing flight. In fixed-wing flight α is small and tends to zero, thus $L\cos\alpha \to L$ and $D\sin\alpha \to 0$. This condition is shown in the free-body diagram presented on the left side of Figure 25. The resulting equation for the moment around the CG (noted M_{CG}) in fixed-wing mode is:

$$M_{CG} = M_w - l_{AC}L + M_{\delta_1}^Y + M_{\delta_2}^Y \tag{11}$$

Taking the derivative of Equation 11 with respect to α, the pitch static stability of the DPA is defined as $C_{M_\alpha} = -l_{AC}C_{L_\alpha}$. Thus, since the CG is always forward to AC in the DPA, the aircraft is static stable in pitch since $C_{M_\alpha} < 0$. In contrast, the analyses of trim, neutral point, and static margin for the fixed-wing mode are out of the scope of the present work.

Figure 25: *Longitudinal free-body diagrams.*

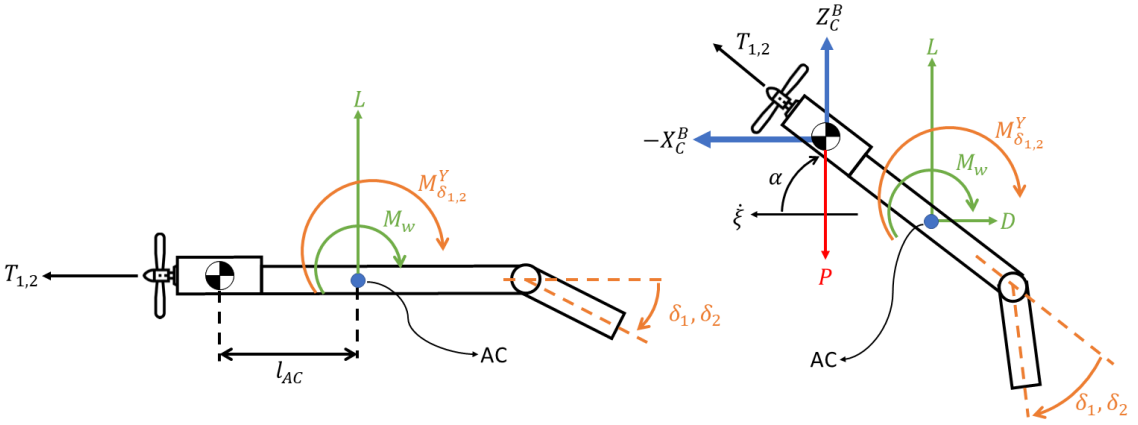

Source: Author.

B.2.2 Lateral-directional analysis

The sum of moments around the CG along the X_C^P axis is based on the free-body diagram presented on the left side of Figure 26. The moment for that axis is mainly affected by the differential thrust from the motors. As such, in rotary-wing flight the terms $M_{\delta_i}^X$, $i = 1,2$ are zero. In fixed-wing flight, the aileron moments are relevant because of aileron coupling around the "fixed-wing yaw angle" due to adverse yaw as described by (RAYMER, 1999). The resulting equations are:

$$\sum M_{X_C^P} = l_m(T_1 - T_2) + M_{\delta_1}^X + M_{\delta_2}^X \tag{12}$$

The moments around the CG along the Z_C^P axis are identical for both flight modes. This is because this axis is affected only by the ailerons acting in differential mode. Due to (V), the difference in angular momentum from the motors is not considered in $\sum M_{Z_C^P}$.

The moments are presented in the free-body diagram on the right side of Figure 26. The resulting equations are:

$$\sum M_{Z_C^P} = M_{\delta_1}^Z + M_{\delta_2}^Z \tag{13}$$

Figure 26: *Lateral-directional free-body diagrams.*

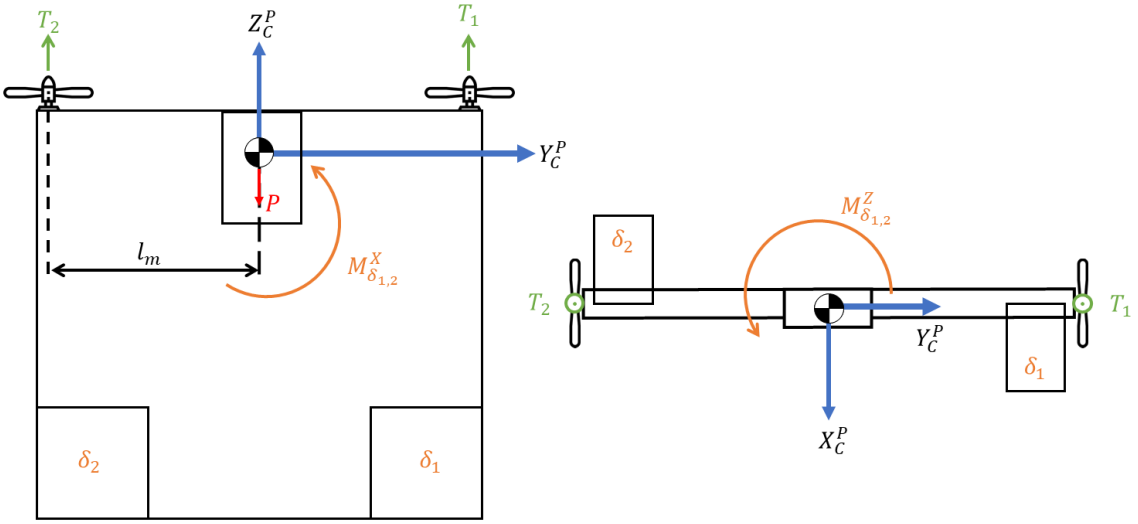

Source: Author.

The present work proposes an aileron convention where the aileron moments $M_{\delta_j}^Y$ are positive (aircraft nose-up, increasing pitch angle) when the aileron deflection $\delta_j,\ j = 1,2$ is positive (to the down face). This causes the $M_{\delta_j}^X$ and $M_{\delta_j}^Z$ moment pairs to present inverse signal values when the ailerons present positive δ_j:

$$\begin{cases} \delta_{1,2} > 0 \implies M_{\delta_{1,2}}^Y > 0 \implies \ddot{\theta} > 0 \\ \delta_1 > 0 \implies M_{\delta_1}^X, M_{\delta_1}^Z < 0 \\ \delta_2 > 0 \implies M_{\delta_2}^X, M_{\delta_2}^Z > 0 \end{cases} \tag{14}$$

B.3 Powerplant modeling

The proposed powerplant model considers the following components: avionics, ESC, motor, and propeller. The ESC of the DPA is controlled by the avionics through an RC standard PWM signal with duty cycle $u_k \in [0,1]$. The ESC provides voltage to the motor as a function of the desired motor rotational speed (noted ω). The ESC manufacturer documents a linear relation between the PWM duty cycle and the motor rotational speed. The motor's shaft is connected to the propeller using a 1:1 direct-coupling. Thus, the propeller rotates at the same ω as the motor, creating thrust.

The blades of a propeller are equivalent to wings producing lift and drag. The thrust produced by a propeller is a function of the lift of the blades while the drag of the blades limits ω. The thrust force presents a dynamic variation as a function of the speed and the propeller pitch. As the speed in the direction of the propeller axis increases, the AoA perceived by the blades and the thrust are reduced (RAYMER, 1999). Due to the mission and (I), such dynamic is neglected in the present work and the available thrust is considered constant and equal to its static value.

The present work bases its propeller and thrust model on the momentum-blade element theory as described in detail in the work of (MCCORMICK, 1995). The total thrust produced by the propeller is a function of ω, ρ, the thrust coefficient (noted C_T), and the propeller diameter (noted D_{prop}) being defined as:

$$T_k = \rho C_T \omega_k^2 D_{prop}^4 \tag{15}$$

B.4 Aileron modeling

The propwash is the only airflow source acting over the ailerons in hover flight due to the mission, the aircraft design, and assumption (I). Thus, to estimate the dynamic pressure on the aileron the propeller-induced speed is used. The works of (MCCORMICK, 1967) and (STONE, 2002a) argue that the flow development (noted Dev_{pw}) to static laminar condition is estimated through the distance between the propeller and the aileron (noted s) and the propeller radius (noted R):

$$Dev_{pw}[\%] = \frac{s}{\sqrt{s^2 + R^2}} \tag{16}$$

This relation tends to 100% as s tends to $+\infty$. Considering the DPA's parameters $R = 0.1143\ m$ and $s = 0.5 - 0.16 = 0.34\ m$, the flow development is equal to $Dev_{pw} = 94.78\%$. Thus, the present work considers a fully developed flow over the ailerons. Moreover, a flow that remains attached to the body is considered fully contracted. This means that, in the DPA's case, the flow is parallel to Z_C^P at least until reaching the aileron. Such condition is true for the DPA considering the discussions from (MCCORMICK, 1967) and (STONE, 2002b). Various works in CUAV with aircraft in conditions similar to the DPA as (KNOEBEL et al., 2006) and (ESCARENO, 2008) consider also that these two conditions are true.

Based on these conditions and assuming an axially contracted, fully developed flow, the momentum theory (or actuator disk theory) as presented in details in (MCCORMICK, 1967) and (MCCORMICK, 1995), and used by (STONE, 2002b), (KNOEBEL et al., 2006) and (ESCARENO, 2008), defines the propeller-induced speed (noted V_{pw}) and propeller-induced dynamic pressure (noted q_{pw}) as:

$$V_{pw} = \sqrt{\frac{2T_k}{\rho \pi R^2}} \implies q_{pw} = \frac{T_k}{\pi R^2} \tag{17}$$

This dynamic pressure is present over the aileron surface inside the contracted propwash. However, in the DPA's case, only a section of the aileron span is placed inside this flow. The surface inside the flow (noted $S_{a,pw}$) is calculated considering the cross-section in the wingtip, the propeller radius and the aileron span, which for the DPA is equal to $S_{a,pw} = 0.15 \cdot (0.1143 - 0.05) = 0.009645\ \text{m}^2$. In contrast, the total aileron surface of the DPA (noted S_a) is equal to $S_a = 0.15 \cdot 0.2 = 0.03\ \text{m}^2$ configuring an area efficiency of 32.15%. In terms of geometry, there are two lever-arms relevant to the aileron moments: the distance l_a between the center of the aileron span and the CG; and the distance $l_{a,\ pw}$ between the center of the span of $S_{a,pw}$ and the CG. In the DPA's case, $l_a = 0.35\ m$ and $l_{a,\ pw} = 0.38215\ m$.

B.4.1 Aileron moments

In conventional layout fixed-wing aircraft design the aileron moments are derived as part of the stability and control analysis. Such equations are based on the fact that an aerodynamic force (a lift) created on the station of the wing where the aileron is placed times a lever-arm (chord or distance in wingspan direction) creates a moment. The present work proposes equations for the aileron moments derived from the same method.

The proposed equations for $M^Y_{\delta_i}$ are based on the moment flaps create on the wing of a fixed-wing aircraft as presented by (RAYMER, 1999) and on the strip theory for ailerons as presented by (RAYMER, 1999) and (KNOEBEL et al., 2006). Such an equation is a function of flight mode in terms of dynamic pressure and reference area:

$$M^Y_{\delta_i} = q(\theta)S(\theta)C^Y_{M_\delta}\delta_i \tag{18}$$

where the product $q(\theta)S(\theta)$ is defined as:

$$q(\theta)S(\theta) = \begin{cases} q_{pw}\, S_{a,pw}, \theta \in [0,-45[\\ \frac{1}{2}\rho V^2 S_a, \theta \notin [0,-45[\end{cases} \tag{19}$$

The term $C^Y_{M_{\delta_i}}$ is the pitching moment derivative with respect to aileron deflection. The works of (STONE, 2002b) and (ESCARENO, 2008) propose a constant $C^Y_{M_{\delta_i}}$ for CUAV-VATOL similar to the DPA. In particular, the work of (KNOEBEL et al., 2006) estimates this derivative through thin airfoil theory as:

$$C^Y_{M_\delta} = \frac{\sin(2\sigma) - 2\sin(\sigma)}{4} \tag{20}$$

where $\sigma = \arccos(2c_a/c - 1)$ considering the aileron chord as c_a.

The equation of $M^Z_{\delta_i}$ is based on the discussions from the works of (ESCARENO, 2008) and (RAYMER, 1999). In the first, the yaw in rotary-wing flight is treated as a difference of lift between the two ailerons while in the second, equations for rolling moments based on aileron strip theory are presented. The resulting equations present a sign difference to comply with the aileron direction convention:

$$M^Z_{\delta_1} = -l(\theta)q(\theta)S(\theta)C_{L_\delta}\delta_1 \tag{21}$$

$$M^Z_{\delta_2} = l(\theta)q(\theta)S(\theta)C_{L_\delta}\delta_2 \tag{22}$$

where the product $l(\theta)q(\theta)S(\theta)$ is defined as:

$$l(\theta)q(\theta)S(\theta) = \begin{cases} l_{a,pw}\, q_{pw}\, S_{a,pw}, \theta \in [0,-45[\\ \frac{1}{2}\rho V^2 S_a l_a, \theta \notin [0,-45[\end{cases} \tag{23}$$

The term C_{L_δ} is the lift force derivative with respect to aileron deflection. The value of this derivative is obtained through the lift coefficients of the STFP with an aileron.

The aileron moments $M^X_{\delta_i}$ are relevant for fixed-wing only and are based on the estimation of adverse yaw proposed by (RAYMER, 1999):

$$M^X_{\delta_2} = -l_a q S C^X_{M_\delta}\delta_2 \tag{24}$$

$$M^X_{\delta_2} = l_a q S C^X_{M_\delta}\delta_2 \tag{25}$$

where $C^X_{M_\delta} = C_L C_{L_\delta}$ is the "fixed-wing yaw" derivative with respect to aileron deflection.

B.5 Inertial positioning

The position of the aircraft is measured in the inertial frame. Let a force F taken in an arbitrary reference frame U be denoted as $\overrightarrow{\mathrm{F}^{\mathrm{U}}}$. The accelerations are described by Newton's 2nd law considering that the resultant of forces taken in the inertial frame is $\sum\overrightarrow{\mathrm{F}^{\mathrm{I}}}$ and the aircraft's mass is m:

$$\sum\overrightarrow{\mathrm{F}^{\mathrm{I}}} = m\ddot{\xi} \tag{26}$$

Since the inertial and body frame have the same orientation, the acceleration can be expressed considering the resultant of forces taken in the body frame:

$$\ddot{\xi} = \frac{1}{m}\sum\overrightarrow{\mathrm{F}^{\mathrm{B}}} \tag{27}$$

The forces acting on the body frame can be decomposed in terms of their dependence on η. Let the unitary vectors related to an arbitrary reference frame U be denoted as $\{i^U, j^U, k^U\}$. The aircraft's weight (noted P) is always in the negative direction of Z^B_C. Thus, the acceleration can be defined as:

$$\ddot{\xi} = \frac{1}{m}(-P\hat{k^B} + R^{P\to B}\sum\overrightarrow{\mathrm{F}^{\mathrm{P}}}) \tag{28}$$

where $R^{P\to B}$ is the rotation matrix that brings forces from the pose frame to the body frame. This matrix is obtained through three consecutive rotations around yaw ψ, pitch θ and roll ϕ in that order. Considering $\sin(x) = S_x$ and $\cos x = C_x$, the rotation matrix is defined as:

$$R^{P\to B} = \begin{bmatrix} C_\theta C_\psi & S_\phi S_\theta C_\psi - C_\phi S_\psi & C_\phi S_\theta C_\psi + S_\phi S_\psi \\ C_\theta S_\psi & S_\phi S_\theta S_\psi + C_\phi C_\psi & C_\phi S_\theta S_\psi - S_\phi C_\psi \\ -S_\theta & S_\phi C_\theta & C_\phi C_\theta \end{bmatrix} \tag{29}$$

Most works about flight stability and control, notably (NELSON, 1989) for fixed-wing aircraft and (ESCARENO, 2008) for CUAV, propose the same rotation matrix to represent forces in the inertial frame.

The sum of forces in the pose frame includes lift, drag and thrust from the two motors. Considering the mission, assumption (VI), and the definition of AoA, such sum is only a function of θ and is defined as:

$$\sum\overrightarrow{\mathrm{F}^{\mathrm{P}}} = (-L\sin\theta + D\cos\theta)\hat{i^P} + (T_1 + T_2 + L\cos\theta + D\sin\theta)\hat{k^P} \tag{30}$$

B.5.1 Simplified altitude

A simplified altitude model is proposed based on Equation 28 and considering assumption (IV). Solving for the term $\hat{k^B}$ of $\sum\overrightarrow{\mathrm{F_B}}$ yields:

$$LS^2_\theta + DS_\theta C_\theta + (T_1 + T_2)C_\phi C_\theta + LC_\phi C^2_\theta + DS_\theta C_\phi C_\theta \tag{31}$$

The acceleration in Z^I_O is obtained from the term of altitude $\hat{k^I}$ from Equation 28 which is defined as:

$$\ddot{z} = \frac{1}{m}(-P + LS_\theta^2 + DS_\theta C_\theta + (T_1 + T_2)C_\phi C_\theta + LC_\phi C_\theta^2 + DS_\theta C_\phi C_\theta) \tag{32}$$

Due to assumption (IV), the static hover condition is applied. Thus, considering $\|\eta\| = 0$ and $\|\dot{\xi}\| = 0$, the resultant altitude dynamics is given by:

$$\ddot{z} = \frac{1}{m}(T_1 + T_2 - P) \tag{33}$$

APPENDIX C - OPEN-LOOP MAIDEN FLIGHT

This chapter reports the results from the prototype's *maiden flight*. During its first flight, the aircraft is manually operated by the author in a controlled environment without any closed-loop control from the avionics. In the DPA's case, the maiden flight serves to analyze the proposed model and its simplification hypotheses. The used avionics did not include sensors or flight computer, and it is composed of only a standard RC radio receiver weighing 0.032 kgf with cabling included. Such avionics are only 19.63% of the estimated weight from section 5.5. This configured an empty-weight of 0.522 kgf and an MTOW of 0.685 kgf, yielding an EWF of 76.2% and a T/W of 1.845.

Based on (II), (VI), and considering a windless controlled environment (as required by the mission) the DPA is expected to take off from a static condition ($\|\eta\| = 0$ and $\|\dot{\xi}\| = 0$) with the altitude and attitude dynamic fully decoupled as proposed by (IV). This implies that the simplified altitude dynamic obtained from the inertial positioning model and represented by Equation 33 could be analyzed isolated and without any attitude closed-loop control in form of stability augmentation systems. The flight plan included only takeoff and landing. Subsequent flights would include hover, then rotary-wing displacement, transitions, and fixed-wing flight at last. The same segmented progression was successfully used by the Pogo's design team.

The prototype was placed in landed position. The throttle would be increased until the aircraft TE left the ground defining a takeoff. This was expected to happen around 73.61% of the throttle. However, the expected takeoff with $\|\eta\| = 0$ was not found because while the throttle was carefully increased an unexpected pitching moment became visible on the aircraft for any throttle over 40%. This moment was in the negative direction (decreasing pitch angle or nose-down) and it caused the tail body of the DPA top face to leave the ground before the rest of the aircraft creating an uncontrolled forward movement. This pitching moment and the resulting forward movement were present for any level of thrust until the takeoff that was obtained with 61.11% of the throttle. A maximum altitude of 15 cm was obtained until the test was aborted due to safety issues from the forward movement.

This phenomenon indicates that some AoA is present at the wing during takeoff creating an aerodynamic pitching moment. The present work proposes that such AoA is created by the propwash. The motors are configured to rotate in opposite directions as described in section 5.2. However, any pair of opposite-direction rotations still presents a different than zero airflow at the center of the wingspan. In the DPA's case, both propellers move from top face to bottom face in the center of the wingspan creating a downwash at the LE. The present work proposes that such flow creates an induced negative AoA which then creates negative lift and pitching moment which were found in the takeoff test. Moreover, the present work analyzed the propwash flow development at the ailerons, not the

whole wing chord. The described downwash at the LE could be considered as a component of a not fully contracted propwash flow in the region of the chord before the ailerons. Thus, these considerations imply that a pitch stability control system is required to enable a safe takeoff and landing even from a static condition in a windless environment.

To address this requirement and allow for the continuation of open-loop manually operated flights, modifications were made in the prototype to increase its inertia I_Y around the Y_C^P axis. To increase the dimension equivalent to the tail span, an EPS sheet measuring 1 m by 1 m was installed in the prototype at the TE creating a square base for the aircraft. The total added weight was equal to 0.317 kgf, configuring a new empty-weight of 0.839 kgf and an MTOW of 1.002 kgf, yielding an EWF of 83.7% and a T/W of 1.261. The throttle level for takeoff in this new MTOW was estimated as 89%.

The modified prototype was placed in landed position. The throttle was carefully increased and the previous pitching moment and forward movement were not observed until the takeoff that was obtained with 88.89% of throttle with a maximum altitude of 10 cm. However, this takeoff presented an unstable movement in roll (around X_C^P) after the aircraft left the ground. This moment indicates that the motors are creating differential thrust or that an unexpected roll perturbation is present. Thus, this implies that a roll stability control system is required to enable a safe takeoff and landing even from static condition in a windless environment. It is proposed that considering the unmodified prototype, if a pitch stability control system was present the unstable roll dynamic would be observed after takeoff. In the case of the present work, the modified prototype was used to expose such dynamics.

During the takeoff of the modified prototype, an additional phenomenon was observed: the unpowered ailerons were moved in the direction of positive δ_j by the propwash after a throttle level of 66.66%. This did not happened during the takeoff of the original prototype which indicates that the designed ailerons are capable of opposing the pitching moment found in the first test if a pitch stability control system was present.

C.1 Design implications

As indicated by the proposed model of the aircraft, the reported unexpected roll movement is created by differential thrust from the motors during the takeoff. In the flight reported, a single PWM control signal was used to control both motors as an equal thrust was desired for takeoff. As equal thrust was not obtained, characterization of both halves of the powerplant is required to detail the relation $u_k \rightarrow T_k$ for each half of the powerplant.

In terms of design choices, a smaller distance between the CG and the motors could decrease the effects of the characteristics of each motor. However, different design definitions would only reduce, not eliminate the differential thrust. The same applies to the tail: a larger tail span could be selected to restrain the unexpected pitching moment while additional tail bodies could increase I_Y.

In conclusion, the maiden flight indicated the need for pitch and roll stability control systems to enable a safe takeoff while validated parts of the aeronautical design, the aircraft concept, and the maneuver methods using the ailerons as well as showed unexpected dynamics. A higher takeoff altitude or the proposed subsequent flight plans were not tested due to safety issues. Such tests can be performed in future works using the required stability control systems.